Tracking timescales of magma reservoir recharge through caldera cycles at Santorini (Greece). Emphasis on an explosive eruption of Kameni Volcano

Antonio Polo-Sánchez, Taya Flaherty, Garance Hervé, Tim Druitt, Gareth N Fabbro, Paraskevi Nomikou, Helène Balcone-Boissard

frontiers | Frontiers in Earth Science

TYPE Original Research
PUBLISHED 22 June 2023
DOI 10.3389/feart.2023.1128083

OPEN ACCESS

EDITED BY
Roberto Sulpizio,
University of Bari Aldo Moro, Italy

REVIEWED BY
Chiara Maria Petrone,
Natural History Museum, United Kingdom
Eugenio Nicotra,
University of Calabria, Italy

*CORRESPONDENCE
Tim Druitt,
tim.druitt@uca.fr

RECEIVED 20 December 2022
ACCEPTED 12 June 2023
PUBLISHED 22 June 2023

CITATION
Polo-Sánchez A, Flaherty T, Hervé G, Druitt T, Fabbro GN, Nomikou P and Balcone-Boissard H (2023), Tracking timescales of magma reservoir recharge through caldera cycles at Santorini (Greece). Emphasis on an explosive eruption of Kameni Volcano.
Front. Earth Sci. 11:1128083.
doi: 10.3389/feart.2023.1128083

Tracking timescales of magma reservoir recharge through caldera cycles at Santorini (Greece). Emphasis on an explosive eruption of Kameni Volcano

Antonio Polo-Sánchez[1,2], Taya Flaherty[1], Garance Hervé[1], Tim Druitt[1]*, Gareth N. Fabbro[3], Paraskevi Nomikou[4] and Helène Balcone-Boissard[5]

[1]Laboratoire Magmas et Volcans, Université Clermont Auvergne OPGC, CNRS, IRD, Clermont-Ferrand, France, [2]Departamento de Geología, Universidad de Salamanca, Salamanca, Spain, [3]School of Environmental Sciences, University of East Anglia, Norwich, United Kingdom, [4]Department of Geology and Geoenvironment, National and Kapodistrian University of Athens, Athens, Greece, [5]UMR 7193 Institut des Sciences de La Terre de Paris (ISTeP), CNRS-Sorbonne Université, Paris, France

Pre-eruptive processes and their timescales are critical information for risk management at explosive volcanoes, and Santorini caldera (Greece) provides an excellent context in which to approach this subject. We ask two questions. First, are pre-eruptive processes the same for small and big eruptions? To investigate, we performed a multi-mineral diffusion timescale study of a small explosive eruption of Kameni Volcano and compared the results with those published for larger caldera-forming eruptions at Santorini. The Kameni dacite resembles products of larger eruptions in being crystal-poor, containing plagioclase with antecrystic cores and autocrystic rims, bearing orthopyroxene with sector zoning and phantom skeletal morphologies, and showing evidence for mixing of different silicic magmas prior to eruption. Diffusion timescales from Mg-Fe profiles in orthopyroxene and clinopyroxene phenocrysts are <1–23 years, and Mg diffusion modelling in plagioclase gives <10 years. Our physical model for the Kameni eruption is similar to those proposed for larger eruptions, where silicic melt produced in gabbroic to dioritic lower to middle crustal mush bodies is transferred (along with entrained mafic magma) to an upper crustal reservoir. Crystals grow in the hydrous silicic melts due to decompression, cooling, and magma mixing during ascent and injection into upper crust. We propose that large eruptions are preceded by similar processes as small ones, but on a larger scale. Our second question: do diffusion timescales relate to eruptive volume or position in a caldera cycle? For this, we obtained orthopyroxene Mg-Fe diffusion timescales for three additional eruptions, growing our orthopyroxene timescale database to seven eruptions of different sizes and cycle timings. No clear relationship exists between diffusion timescale and volume; however, timescales are systematically shorter (<0.01–10 years) early in a cycle and longer (1–5,000 years) late in a cycle. Thermal maturation and H_2O-flushing of the crustal magma reservoir through the caldera cycle could explain this, as the reservoir would change from a rigid to more mushy state as the cycle progresses. This would change the mechanical response to melt input and allow accumulation

of progressively larger melt layers in the upper crust, resulting in increasing crystal residence times.

KEYWORDS

diffusion timescales, Kameni, Santorini, caldera cycles, pyroxene

1 Introduction

Silicic caldera systems operate in cycles consisting of long periods of minor volcanism that culminate in large-magnitude caldera-forming eruptions (Smith and Bailey, 1968; Cole et al., 2005; Bouvet de Maisonneuve et al., 2021). The processes governing caldera cycles are not well understood, and predicting the outcome of a given unrest event - no eruption, small eruption, or Plinian eruption - remains a challenge. One parameter of interest is the timescale of recharge of the magmatic system prior to eruption. Studies have shown that caldera magmatic systems have long periods of repose, punctuated by relatively short periods of recharge (Druitt et al., 2012; Parks et al., 2012) that lead to geophysical and geochemical signals that can be detected at Earth's surface (Newhall and Dzurisin, 1988; Acocella et al., 2015; Singer et al., 2018).

Silicic magmatic systems are transcrustal, with regions of melt generation and storage throughout the crust (Cashman et al., 2017). Silicic melts are believed to be generated and stored for long periods in crustally hosted mush bodies (Koyaguchi and Kaneko, 1999; Hildreth, 2004; Cooper and Kent, 2014; Bachmann and Huber, 2016). Rejuvenation of a crustal magmatic system prior to eruption can involve heat transfer, input of mantle-derived mafic melts and fluids, amalgamation of silicic melt lenses, compaction of mushes, or mixing of melts and crystals (Cashman and Blundy, 2013; Bergantz et al., 2015; Bachmann and Huber, 2016; Cashman et al., 2017; Bachmann and Huber, 2019; Sparks et al., 2019). Mush reorganization can cause vertical transfer of melts and fluids that recharge shallow storage chambers and increase pressure sufficiently to trigger eruptions or periods of unrest. The recharge magmas may be mafic or compositionally more evolved. Mafic magmas quench in silicic magmas to form mafic enclaves, whereas mixing of two more evolved magmas leaves evidence that is petrologically more cryptic (de Silva et al., 2008; Druitt et al., 2012; Balcone-Boissard et al., 2018). Recharge events are recorded in crystals as perturbations in the pressure-temperature-composition (P-T-X) environment, generating zones of growth, resorption and diffusive re-equilibration (Allan et al., 2017; Fabbro et al., 2017; Costa et al., 2020; Metcalfe et al., 2021; Ostorero et al., 2021; Elms et al., 2023).

Diffusion gradients in crystals have been central to estimating pre-eruptive recharge timescales (Costa et al., 2020). During recharge, moving melts can pick up antecrysts from surrounding mushes and precipitate new crystals due to decreases in temperature, pressure, or H_2O activity. Mixing of a hotter magma with a cooler magma can also cause crystal growth in the hotter magma. Growth zoning in a crystal relaxes with time due to diffusion, the rate of which depends on the chemical species concerned, and measured diffusion profiles can be inverted through modelling to estimate the timescales of crystal P-T-X perturbations prior to eruption (Morgan et al., 2004; Saunders et al., 2012; Allan et al., 2013; Costa et al., 2013; Chamberlain et al., 2014; Kilgour et al., 2014; Petrone et al., 2016; Fabbro et al., 2017; Krimer and Costa, 2017; Solaro et al., 2020; Metcalfe et al., 2021; Ostorero et al., 2021; Mangler et al., 2022). The modelling requires estimates of crystal residence temperature, along with a petrological context in which to interpret the timescales obtained. A common approach is to calculate the diffusion timescale at the pre-eruptive magma temperature given by geothermometers (e.g., Fabbro et al., 2017). Another method employs non-isothermal modelling by estimating temperature changes during crystal growth and diffusion (Druitt et al., 2012; Petrone et al., 2016). Crystals record a range of diffusion timescales depending on the mineral and diffusing elements, but systems like Mg or Sr in plagioclase or Mg-Fe exchange in orthopyroxene (opx) and clinopyroxene (cpx) typically record timescales of months to millenia (Costa et al., 2020).

Previous studies at Santorini have used diffusion geochronometry of multiple mineral species (Mg-Fe diffusion in opx, Mg-Fe diffusion in cpx, Mg and Sr diffusion in plagioclase) in the products of two silicic caldera-forming eruptions (22 ka, 3.6 ka) and in a sequence of inter-Plinian lavas (39–25 ka) preceding the 22 ka caldera-forming one, all of which occurred late in a caldera cycle. The resulting diffusion timescales in all three cases ranged from millenia to years, and were interpreted as the timescales of pre-eruptive recharge (Druitt et al., 2012; Fabbro et al., 2017; Flaherty et al., 2018).

In the present paper we ask questions concerning two important but poorly understood issues. (1) Are the processes leading up to small eruptions the same as for large eruptions? (2) How do reservoir recharge timescales vary with eruption magnitude and throughout a caldera cycle? To address question 1, we carried out a petrological and multi-mineral diffusion modelling study of a small silicic eruption using the same approaches as in our previous works on Santorini caldera-forming eruptions. For this we chose a small explosive eruption of Kameni Volcano situated inside Santorini caldera (Barton and Huijsmans, 1986; Pyle and Elliott, 2006; Higgins et al., 2021). We present a study of the crystal cargo of the eruption, and measure diffusion timescales in three mineral systems (Mg-Fe in opx, Mg-Fe in cpx, Mg in plagioclase). We then compare and contrast the results with those from our previous studies of larger eruptions. To address question 2, we present a less detailed study of opx Mg-Fe diffusion timescales from two additional early-cycle silicic eruptions and another late-cycle caldera-forming eruption in order to increase the size of our opx database. We then integrate the results with those published previously to generate an internally coherent dataset of opx diffusion timescales for seven eruptions ranging from ~0.1 to 40 km^3 DRE at this single, caldera-forming system.

2 Geological background

Santorini lies on the South Aegean Volcanic Arc within the Pliocene-to-present Christiana-Santorini-Kolumbo Volcanic field

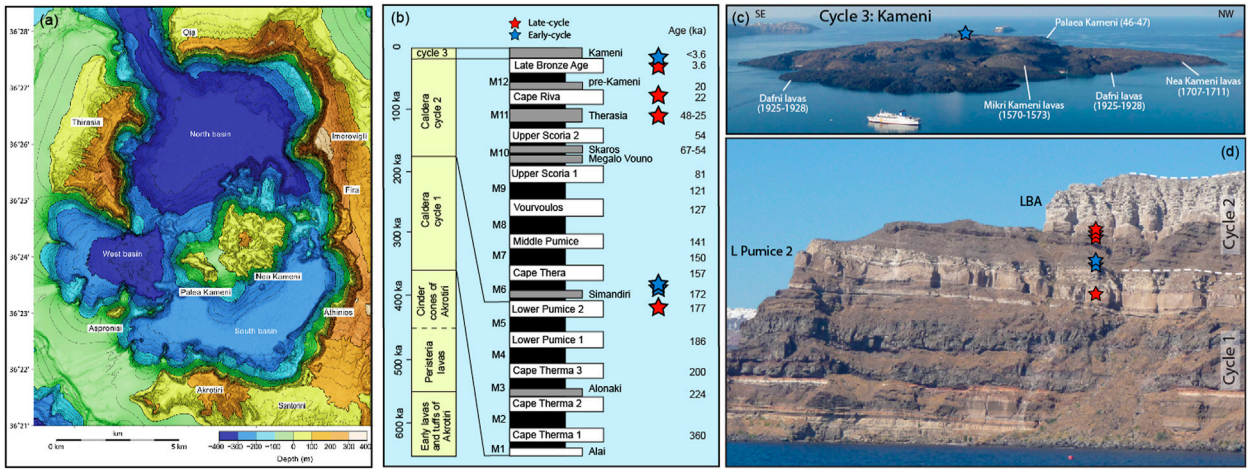

FIGURE 1
(A) Digital onshore and offshore elevation model of Santorini caldera (after Nomikou et al., 2014). **(B)** Volcanic history of Santorini, with an enlargement of the two explosive cycles since 360 ka. White units, Plinian eruptions; black units, inter-Plinian sequences of lavas and minor pyroclastics (numbered 'M' for minor); grey units, major effusive episodes within the inter-Plinian sequences. The activity of the last 360 ka can be divided into two major caldera cycles, each ending with a pair of silicic caldera-forming eruptions (Lower Pumices 1 and 2 in cycle 1, Cape Riva and Late Bronze Age in cycle 2). The coloured stars show the eruptions included in the present paper (blue, early cycle; red, late cycle). **(C)** The Kameni islands showing the location (star) of the PKP sample collected. **(D)** The caldera cliffs showing the stratigraphic locations (stars) of the other sampled eruptions in panel B. The location of this headland is 2 km south of Fira town on Panel A.

(Nomikou et al., 2018; Vougioukalakis et al., 2019; Preine et al., 2022). The volcanic field is hosted by a NE-SW-trending en-echelon rift system formed by arc-parallel extension (Nomikou et al., 2018). Santorini is a 10 km north-south, 8 km east-west caldera with its floor 390 m below sea level (Figure 1A) (Nomikou et al., 2014). It has been active since at least 650 ka, and since 360 ka has had ~100 explosive eruptions (Figure 1B) (Druitt et al., 1999; Kutterolf et al., 2021). Twelve prominent Plinian eruptions are named, and the sequences of minor inter-Plinian tephra and lavas between them are numbered ('M' for minor; Figure 1B). These are organized into two main caldera cycles, from ~360 to 177 and 177 to 3.6 ka. Each cycle began with many explosive eruptions in the 0.1–10 km^3 DRE (Dense Rock Equivalent) range alternating with periods of lava effusion, and culminated in a pair of 10–40 km^3 DRE silicic, caldera-forming eruptions (Lower Pumices 1 and 2 of cycle 1; Cape Riva and LBA of cycle 2). The historically active Kameni volcano within the caldera is interpreted as the start of caldera cycle 3.

The Kameni edifice is 470 m high, with a basal diameter of 3.5 km and a volume of 4.3 ± 0.7 km^3 (Figure 1A) (Nomikou et al., 2014). Ten eruptions of Kameni have been recorded since 197 BCE, with seven since the 16th century (Figure 1C) (Pyle and Elliott, 2006). In March 2011, Santorini entered a 15-month period of bradyseismic unrest, involving increased microseismicity along a NE-SW fault line beneath Nea Kameni, uplift of Santorini by up to a few cm, and increased gas emission from fumaroles. This has been attributed to the intrusion of about 14 × 10^6 m^3 of magma in two pulses (Parks et al., 2015). Modelling has showed a pressure source situated ~1 km north of Nea Kameni and at 4.4 ± 1.0 km depth beneath the seafloor (Parks et al., 2012; Parks et al., 2015). Rare gas isotopic studies support a magmatic origin for the uplift (Rizzo et al., 2015).

Santorini lies on rifted continental crust about 25 km thick and is fed by mantle-derived basalts ranging from tholeiitic to calc-alkaline in character (Flaherty et al., 2022). Fractionation of these basalts in a transcrustal magmatic system (Druitt et al., 2016) generates intermediate and silicic melts that are transferred upwards to shallow holding reservoirs from which they either erupt or crystallise to form plutons (Cottrell et al., 1999; Druitt et al., 1999; Zellmer et al., 1999; Cadoux et al., 2014; Andújar et al., 2015; Andújar et al., 2016; Flaherty et al., 2018). High-resolution seismic tomography has imaged a shallow reservoir of crystal mush containing at least a few percent of melt at 2.8–5 km below the floor of Santorini caldera (McVey et al., 2020). It is interpreted as the shallow reservoir of Kameni Volcano, and its centre coincides with the pressure source of caldera-floor inflation in 2011–12. This reservoir is shifted slightly north of the Kamenis.

3 The eruptions studied

The Kameni pumice fall deposit studied in this paper was sampled on Palaea Kameni island, where it forms a mantle up to 50 cm thick atop the lava flow interpreted as that of the 46–47 CE eruption (Fytikas et al., 1990). We refer to it as the Palaea Kameni Pumice (PKP). It has been tentatively interpreted as the deposit from the 726 CE explosive eruption, the only significant explosive eruption of Kameni recorded historically (Vougioukalakis et al., 2016). The total volume of the PKP is poorly constrained. Distal ash from the Kameni edifice mapped in deep-sea sediments southeast of Santorini (Kutterolf et al., 2021) has a volume of 0.4 km^3 DRE; it may correlate with the PKP or with several eruptions of Kameni, but it provides a maximum volume estimate for the PKP. In this paper we take the volume of the PKP to be of the order of ~0.1 km^3, but the exact value does not affect our conclusions. If it took place in 726 CE, the PKP eruption was preceded by a repose period of seven centuries following the eruption of 46–47 CE (Pyle and Elliott, 2006; Watts et al., 2015).

TABLE 1 The seven eruptions of this study.

Eruption	Age (ka)	Cycle	Early/Late	Volume (km^3)	Mineral timescales	Source[c]
Kameni (PKP)	726 CE	3	Early	~0.1[a]	opx, cpx, plag	This study
Late Bronze Age	3.6	2	Late	32[a]	opx, cpx, plag	D 2012; Fl 2018
Cape Riva	22	2	Late	39[a]	opx, plag	Fa 2017
Therasia	25	2	Late	~0.2[b]	opx, plag	Fa 2017
M6b	~160	2	Early	~0.1	opx	This study
M6a	~160	2	Early	~0.1	opx	This study
Lower Pumice 2	177	1	Late	11.6[a]	opx	This study

[a]Minimum volumes from Kutterolf et al. (2021) based on marine tephra volumes.
[b]Approximately one-tenth of the ~2 km^3 volume of the entire Therasia lava succession (Fabbro et al., 2017).
[c]Druitt et al., 2012 (D 2012); Fabbro et al., 2017 (Fa 2017); Flaherty et al., 2018 (Fl 2018).

Two additional early-cycle pumice fall deposits (M6a and M6b; both 20 cm thick) were sampled from the M6 inter-Plinian unit at the base of caldera cycle 2, and the pumice fall deposit of the caldera-forming Lower Pumice 2 eruption was sampled at the top of cycle 1 (Figure 1B). These eruptions were studied only for opx diffusion timescales. The volumes of the two M6 pumice falls are poorly constrained, but modelling of sub-Plinian eruptions from Santorini (Jenkins et al., 2015) reproduces approximately the thicknesses of these units and suggests volumes of ~0.1 km^3.

The features of these and previously studied eruptions are listed in Table 1.

4 Materials and methods

The eruptions were studied using descriptions of mineral zoning patterns and multi-mineral diffusion modelling (Mg-Fe in opx and cpx, and Mg in plagioclase): the same techniques as for the 22 and 3.6 ka caldera-forming eruptions (Druitt et al., 2012; Fabbro et al., 2017; Flaherty et al., 2018).

The most pumiceous clasts of each eruption were gently crushed and sieved, the 250 and 125 μm (opx and cpx) and 450 μm (plagioclase) size fractions were separated, and the crystals were concentrated by panning in water. Complete (glass-coated) crystals of opx, cpx and plagioclase were then picked by eye under a binocular microscope. The crystals were mounted in epoxy resin in brass rings, then polished until sectioned approximately through the crystal centre.

Mineral zoning textures were studied using greyscale back-scattered electron (BSE) images obtained with a Bruker JSM-5910 electron microscope. Low resolution images were taken at 16 μs/point and 50 s acquisition time, and high-resolution images at 64 μs/point and 30 min acquisition time. Greyscale levels on the BSE images were analysed using the ImageJ software package (Rasband, 1997) and a 20 μm spot size. Spot mineral analyses were made using a CAMECA SXFive TACTIS LaB6 electron microprobe with 15 kV accelerating voltage, 40 nA beam current and 1–2 μm beam size.

We integrated the new data with previously published Fe-Ti oxide data and the volatile contents of plagioclase-hosted melt inclusions (Druitt, 2014; Druitt et al., 2016).

4.1 Pyroxene

Between 127 and 159 opx crystals were studied by BSE imagery in each of the eruptions, but cpx crystals (13) were studied only in the PKP eruption. Low resolution BSE images of the pyroxene crystals were used to classify them according to their textures and zoning patterns; crystals representative of the different populations were then imaged at high resolution. Only crystals judged by visual inspection to be symmetrically mounted and polished through their centres were imaged. All the crystals had their long axes parallel to the surface of the grain mount. The high-resolution BSE images were calibrated for Mg number (Mg# = 100 × Mg/[Mg+Fe] atomic) using 6 to 14 electron microprobe spot analyses. Correlations between Mg# and greyscale were good (R^2 fits of >0.95 for most, R^2 fits of >0.7 for all), even for cpx (R^2 fits of >0.8 for most, R^2 fits of >0.7 for all), showing that BSE grey levels for cpx are controlled principally by Mg-Fe exchange provided that the range of Ca content is limited (Morgan et al., 2004; Petrone et al., 2016). High-resolution profiles of Mg# across zone boundaries in the pyroxene crystals were made using the calibrated BSE images, and these were used for diffusion modelling. Compositional (Al, Ca, Mg, Fe) maps were made of selected opx crystals.

Diffusive Mg-Fe re-equilibration timescales were determined for opx and cpx using binary element diffusion modelling of Mg-Fe profiles across inter-zonal boundaries (Morgan et al., 2004; Morgan et al., 2006; Allan et al., 2013; Chamberlain et al., 2014; Barker et al., 2016; Allan et al., 2017). We implemented an analytical solution to the one-dimensional diffusion equation, assuming a step function initial boundary condition in Mg#, then fitted the measured profiles by a least squares method, with maximum and minimum uncertainties and a correlation index, R^2. Diffusion modelling was carried out perpendicular to crystal length (c axis) in both pyroxene species at the pre-eruptive temperature given by coexisting Fe-Ti oxides in the groundmass glass (touching pairs where possible). The diffusion coefficient of Dohmen et al. (2016) was used for opx and that of Müller et al. (2013) for cpx, with corrections for diffusion anisotropy of opx and cpx explained in Supplementary Material S1. The timescale derived by modelling of Mg-Fe diffusion across a particular zone boundary is the time elapsed between zone boundary formation and eruption quench, at the assumed temperature of residence. Diffusion timescales obtained by 1D modelling are maximum estimates of the real 3D values (Costa et al., 2008). However, modelling along short

profiles perpendicular to the long (c) axis in prismatic crystals is pseudo-1D, reducing overestimation. By assuming an initial step function, the approach ignores the presence of any growth zoning, also resulting in an overestimation of diffusion time (Costa et al., 2008; Brugman et al., 2022). Attempts to use gradients in Al (which diffuses much slower than Mg-Fe in opx; Nakagawa et al., 2005) to distinguish between growth and diffusive zoning were not helpful, because the Al compositional images are not of high enough resolution and many of our Mg-Fe diffusion profiles are as narrow as 2–3 μm. A full account of the pyroxene diffusion modelling is given in Supplementary Material S1.

Uncertainties on the opx and cpx diffusion timescales are evaluated in Supplementary Material S1. Uncertainties on the opx and cpx timescales based just on the best-fit diffusion length scale are typically ±10–30 %. Including uncertainties on Fe-Ti oxide temperature estimates (taken as ±15 °C), and diffusion parameters increases the total uncertainty on the timescale to ±200–250 %.

4.2 Plagioclase

Plagioclase crystals were studied only in the PKP. Zoning patterns were studied by BSE imagery first at low resolution in 180 crystals. Then, only crystals judged by visual inspection to be symmetrically mounted and polished through their centres were imaged at high resolution. The high-resolution images were calibrated for An content (An = 100 × Ca/[Ca+Na+K] atomic) using several electron microprobe spot analyses per crystal. Modelling of Mg diffusion profiles was attempted in seven plagioclase crystals using the approach of Costa et al. (2003) and Druitt et al. (2012), but only one crystal proved to be strongly zoned enough for this to give a meaningful timescale. The method and result for this one crystal are described in Supplementary Material S1.

5 Terminology

In this paper, we use the crystal terminology of Zellmer (2021). Macroscopic (>~0.5 mm) crystals, or zones within them, are distinguished genetically as autocrystic (crystallized form a melt similar to the carrier melt), antecrystic (crystallized from a different, but genetically related, melt), or xenocrystic (foreign).

We distinguish the 'edge' composition of a crystal (in contact with the groundmass glass) from its internal zones. Some crystals contain distinct cores and rims, where the 'core' is a compositionally and/or texturally distinct entity commonly (but not always) delimited by a major resorption surface, and the 'rim' is the same as the interiors of the core-free crystals.

6 Results for the PKP eruption

6.1 General features of the PKP pyroclasts

The dacitic pyroclasts from the PKP range from white and finely vesicular to black and dense. Intermediate types consist of banded vesicular and dense dacite, probably due to differential outgassing and compaction. The different lithologies differ only in their vesicularity, not in their macroscopic crystal content (5–10 vol%; Higgins et al., 2021) or mineralogy (plag, cpx, opx, Fe-Ti oxides). Macroscopic crystals occur both singly or as loose mono- or poly-mineralogical clusters. The present study focused on the uniformly vesicular pyroclasts. The pyroclasts contain a small percentage (<1 vol%) of mm-sized aphyric mafic enclaves consisting of microlites of plagioclase, augite, and Fe-Ti-oxide in vesicular glass, resembling the type A-1 enclaves of Martin et al. (2006).

6.2 Orthopyroxene

Orthopyroxene crystals occur as elongated, typically euhedral, prisms with aspect ratios up to 6 and compositions of $Wo_{2-3}En_{40-67}Fs_{31-58}$ (Mg# 41–68) (Supplementary Material S2). Two main populations are recognized (Figures 2A–C; Figure 4).

Type 1. The majority (~95 %) of opx crystals are euhedral, with edge compositions of Mg# 63–65 and internal zones of Mg# 58–68. The internal zoning includes normal, reverse, and oscillatory zones, commonly with subtle resorption surfaces; it is not practical to break out subpopulations based on internal zoning patterns. The exceptions are (i) a crystal that has a strongly corroded Fe-rich core (Mg# 48–52) overgrown by a rim of Mg# 61–62 (opx PKB 13–3; Figure 2B), and (ii) a crystal with a well-defined, corroded core of Mg# 61–62 overgrown by a rim of Mg# 66–68 (opx PKB 5–8; Supplementary Material S2). About one quarter of the type 1 opx crystals exhibit sector zoning. This is commonly visible on BSE images (Figure 3A), but is especially visible on maps of Al content (Figure 3B). Al is a slowly diffusing element in opx and records the original textures of the crystal even if Mg and Fe have diffused significantly. Images show relative enrichment of Al on [001] zones of the prismatic crystals (Figure 3B). Sector zoning in opx has been shown experimentally to record high growth rates (Schwandt and McKay, 2006) with differential incorporation of Al on different zones. Many of the sector zoned crystals also have a central line of melt inclusions (Figure 3A). This may imply initial skeletal growth followed by infilling of the skeletal morphology causing entrapment of melt. Overall one half of the type 1 opx crystals exhibit sector zoning and/or a central line of melt inclusions.

Type 2. Two opx crystals are markedly more Fe-rich, with internal compositions of Mg# 48–60 converging on euhedral edges of Mg# 52–54. These also have central lines of melt inclusions (e.g., Figure 2C).

Three remaining opx crystals (not illustrated) have complex zoning patterns, broad compositional ranges (Mg# 41–68) and are subhedral to anhedral in shape, suggesting a xenocrystic origin. This is confirmed by the presence in one of augite exsolution lamellae, showing that the crystal was derived from plutonic rock.

6.3 Clinopyroxene

Clinopyroxene crystals are elongated, typically euhedral, prisms with aspect ratios up to 4.5 and compositions of $Wo_{38-43}En_{34-42}Fs_{14-26}$ (Figures 2D–F; Figure 4; Supplementary Material S2). As for opx, two main populations were identified.

Type 1. About 90 % (12 out of 13) of the crystals have subhedral to euhedral edges with Mg# of 67–69, and oscillatory zoned interiors with Mg# of 64–71. Four of these crystals are cored: one with a euhedral

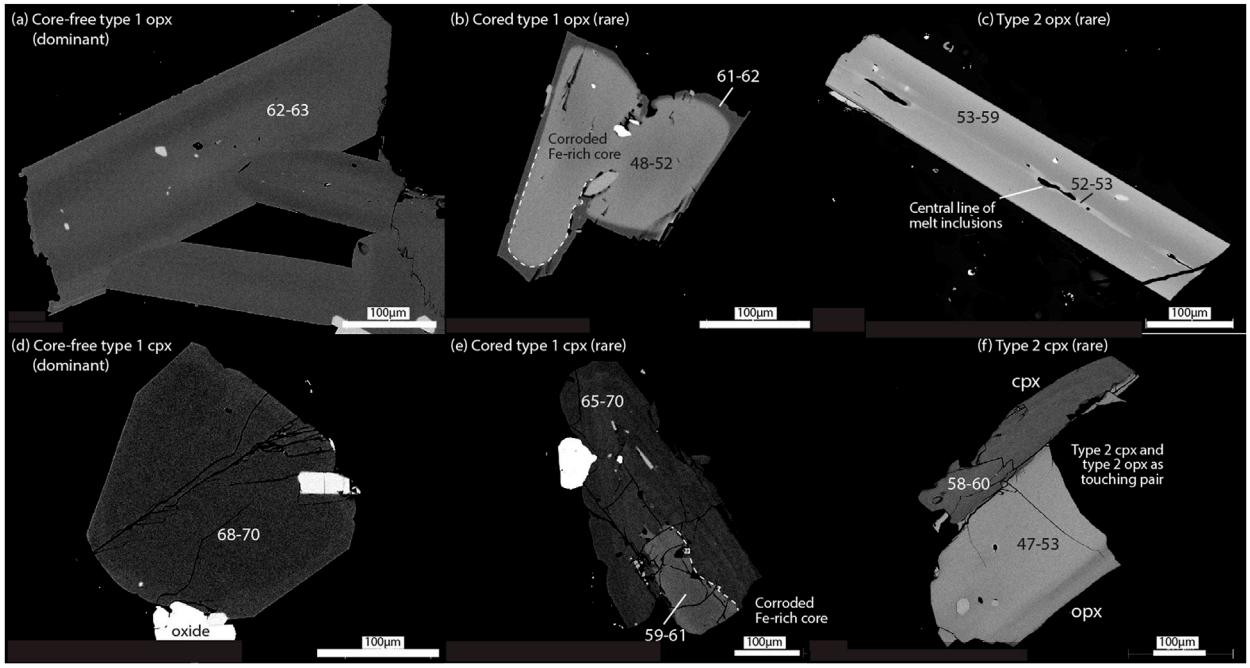

FIGURE 2
(A–C) Orthopyroxene crystals and **(D–F)** clinopyroxene crystals from the PKP. For each pyroxene, three crystal types are illustrated: core-free type 1, cored type 1, and type 2. The numbers give the Mg# (Mg number = 100 × Mg/[Mg+Fe] atomic) values of the different crystal zones. Samples: A opx PKB 1–12, B opx PKB 13–3, C opx PKB 4-6, D cpx PKB 9–13, E opx-cpx pair PKB 8-6, F opx-cpx pair PKB 12–4.

(non-corroded) relatively magnesian cpx core (Mg# 72–74) (cpx PKB 11–4; Supplementary Material S2), and three with partly corroded, relatively Fe-rich cpx cores (Mg# 59–64) (Figure 2E). One type 1 cpx was observed attached to a type 1 opx, suggesting equilibrium between the two (opx-cpx pair 8–6, Supplementary Material S2).

Type 2. A single euhedral cpx is more Fe-rich than type 1, with oscillatory zoned Mg# 58–60 and an edge with an Mg# of 60. It was attached to a type 2 opx, again suggesting an equilibrium relationship (Figure 2F).

6.4 Plagioclase

Plagioclase crystals have compositions of An_{24-66}, and also fall into two main populations (Figure 4; Figure 5).

Type 1. Most (~85 %) of the crystals have internal compositions of An_{39-55}, converging on euhedral edges of An_{48}. They commonly exhibit up to three sawtooth zones, each consisting (in the rimward direction) of (1) a minor resorption surface, (2) a ~10 % increase in An content, (3) normal zoning prior to (4) the next resorption surface or crystal edge (Figure 5D). Oscillatory zoning with fluctuations of ±2–3 % An also occurs, sometimes superimposed on the sawtooth patterns. About a third of type 1 plagioclase crystals have compositionally and texturally distinct cores with corroded shapes: patchy-zoned cores of An_{36-52} (3 crystals), calcic cores of An_{53-66} (2 crystals), and sodic cores of An_{30-43} (6 crystals); the An_{39-55} plagioclase typical of type 1 forms the rims of these crystals. The euhedral outer edges of all type 1 crystals are overgrown by thin (~10 µm) microlitic overgrowths with the same compositions as the groundmass microlites (~An_{50}).

Type 2. Four weakly zoned plagioclase crystals have more sodic compositions (An_{26-34}), subhedral shapes, and distinctive surface textures indicative of dissolution-reprecipitation (Figure 5C). The crystal edge is corroded and overgrown by ~10 µm-sized dendrite-like growths of An_{36-45}.

6.5 Groundmass glasses compositions

Groundmass glasses exhibit a small but distinct heterogeneity, from 70 to 72.5 wt% SiO_2 (Table 2). The less evolved glasses are much more abundant than the more evolved ones. Most type 1 crystals have adhering glass of the less evolved composition; some of the more evolved glasses are associated with type 2 crystals.

6.6 Pre-eruptive volatile contents and intensive parameters

Pre-eruptive temperatures and oxygen fugacities were reported by Druitt (2014) on six touching magnetite/ilmenite pairs in a pumice from the PKP. The results obtained were 905°C ± 3°C and $10^{-6.9\pm0.1}$ Pa using the algorithm of Andersen and Lindsley (1988; software ILMAT, Lepage, 2003), and 926°C ± 5°C and $10^{-6.5\pm0.1}$ Pa using that of Ghiorso and Evans (2008).

Druitt et al. (2016) measured H_2O and CO_2 contents of melt inclusions in five typical type 1 plagioclase crystals by Secondary Ion Mass Spectrometry. The melt inclusions were encased in plagioclase of composition An_{49-52}; they were 50–100 µm in diameter, glassy

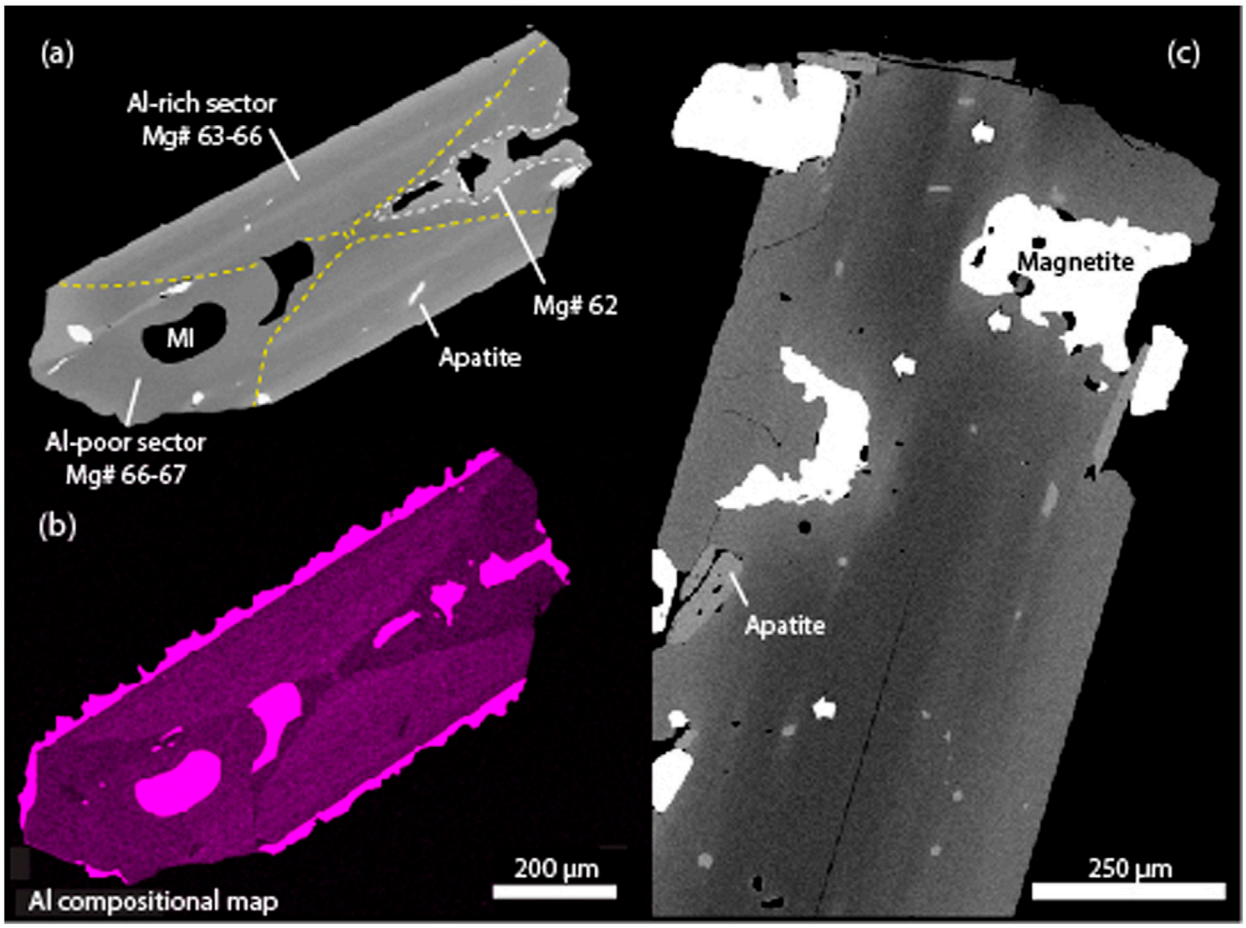

FIGURE 3
Back-scattered images of **(A)** a sector zoned opx with central melt inclusion line indicative of initial skeletal growth followed by filling in of the crystal to form a prism (PKP), **(B)** an Al compositional map of the same crystal, and **(C)** streaky zoning (white arrows) in an opx from the Lower Pumice 2 eruption. MI: melt inclusion. Mg#: Mg Number = 100 × Mg/[Mg+Fe] atomic. Samples: A,B opx PKB 2-5.

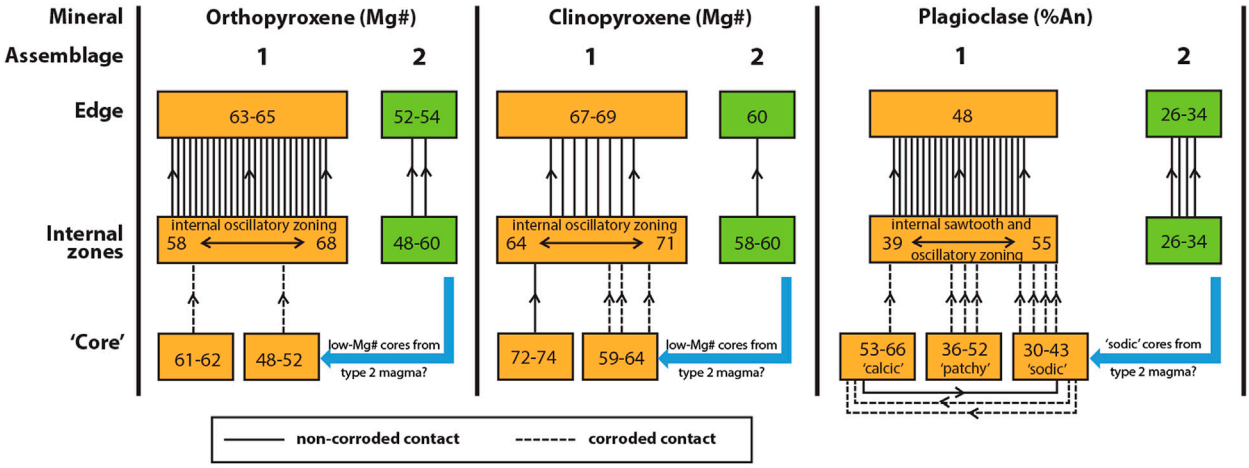

FIGURE 4
Summary of the zoning patterns in opx, cpx and plagioclase of the PKP, from core to crystal edge. The numbers are Mg# Numbers (for opx and cpx) or An contents (for plagioclase). Arrows show the inclusion of one compositional group within another, associated with a conformable (solid arrow) or corroded (dashed arrow) contact. Orange boxes are compositions within type 1 crystals, and green boxes are those within type 2 crystals. The blue arrows show evidence for the inclusion of type 2 crystals as cores within some type 1 crystals.

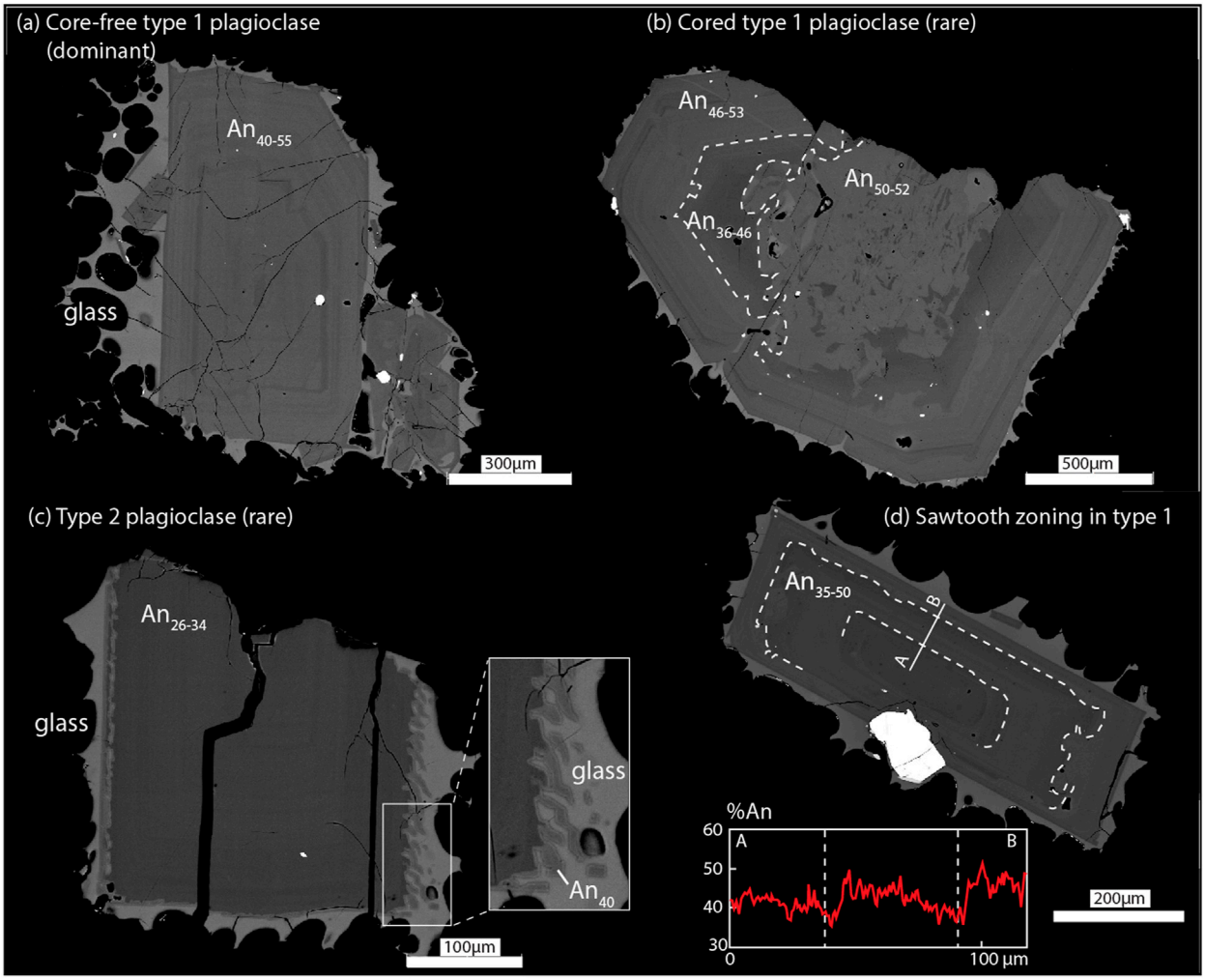

FIGURE 5
Examples of plagioclase zoning types in the PKP. **(A)** core-free type 1, **(B)** cored type 1, **(C)** type 2, **(D)** example of sawtooth zoning from a type 1 crystal. Prominent resorption surfaces are shown as dashed lines.

and crack-free and each contained a single shrinkage bubble. H_2O contents ranged from 4.1 to 5.2 wt%, and glass CO_2 contents (i.e., excluding any CO_2 in the shrinkage bubble) from 40 to 140 ppm. Fluid saturation pressures calculated using the H_2O-CO_2 solubility model of Papale et al. (2006) ranged from 113 to 159 MPa (see Druitt et al., 2016 for full discussion). Druitt et al. (2016) argued, based on a large set of volatile data, that most Santorini magmas are volatile saturated. The H_2O + CO_2 saturation pressures can therefore be converted into depths of 4.3–6.0 km, using a realistic upper crustal density beneath Santorini (2,640 kg m^{-3}; Konstantinou, 2010). This is a minimum depth, since it does not take into account any CO_2 in the shrinkage bubbles.

6.7 Crystal diffusion timescales, PKP eruption

Modelling of diffusion timescales was carried out on 28 opx crystals (69 profiles) and 11 cpx crystals (54 profiles), mainly on the type 1 crystals, which is a dominant assemblage, with one type 2 opx and one type 2 cpx. Representative diffusion profiles and models are shown in Figure 6, and all of them are shown in Supplementary Material S3 and listed in Supplementary Material S4. The aim was to estimate the residence times of the crystals prior to eruption quench. We distinguished between two types of diffusion profile: (i) those across the core-rim boundary of the cored crystals, and (ii) those within the interiors of core-free crystals, or the rims of cored crystals. Diffusion profiles of type (i) yield crystal residence times since core overgrowth, and those of type (ii) give partial estimates of those same residence times.

Modelling was carried out as described earlier, assuming a constant temperature of 905°C, which is the lower estimate of pre-eruptive temperature given by Fe-Ti oxides. By assuming the lower temperature we maximize the calculated diffusion timescales. Although some of the inter-zonal compositional profiles within the crystals may be due to growth, the assumption of a diffusion origin gives maximum timescale estimates (Costa et al., 2008). In the case of the sector zoned opx, the sector zoning is of course of growth origin and our diffusion profiles are across oscillatory zones within

TABLE 2 Representative glass analyses (renormalized, dry).

	mt10 63–4 pt1	mt5 33–4 pt2	mt9 58–2 pt3	mt9 58–2 pt2
SiO_2	70.25	70.31	71.80	72.35
TiO_2	0.66	0.67	0.49	0.35
Al_2O_3	14.40	14.42	13.90	13.84
FeO	3.58	3.68	3.37	3.19
MnO	0.15	0.19	0.11	0.08
MgO	0.67	0.72	0.53	0.45
CaO	2.49	2.48	2.02	1.79
Na_2O	5.32	5.06	5.17	5.30
K_2O	2.41	2.41	2.50	2.49
P_2O_5	0.07	0.07	0.12	0.17

the sector zones. The assumption here is that the sector zoned crystal first grew, then the individual oscillatory zones within it were smoothed by diffusion (Fabbro et al., 2017).

Diffusion timescales for type-1 opx range from <1 to 23 years (with over half the values <5 years), and those for type-1 cpx from <1 to 8 years. The data from opx and cpx are therefore mutually consistent and imply that type-1 pyroxene growth began about a decade or two prior to eruption and continued until eruption. Multiple zone boundaries in a single type 2 opx and in a single type 2 cpx gave timescales of 1–2 years and 1–5 years, respectively: similar to the type-1 pyroxene crystals (Figure 6).

Despite being calculated at a single temperature, these decadal to annual crystal residence timescales are probably geologically meaningful. The diffusion coefficients for Mg-Fe exchange in pyroxenes are very sensitive to temperature (Supplementary Material S1). Referring to phase equilibria experiments on Santorini magmas (Andújar et al., 2016), the compositional ranges of opx and cpx exploited for diffusion modelling above reflect a temperature variation of ±30°C, all other things constant. Plugging this into the diffusion coefficients for opx and cpx results in a ± variation on opx and cpx timescales of about a factor of two; this is comparable to the effect on diffusion timescales of the inherent uncertainties of Fe-Ti oxide temperatures and of diffusion thermodynamic parameters (Supplementary Material S1). It justifies the assumption of a single temperature for diffusion timescales in our study.

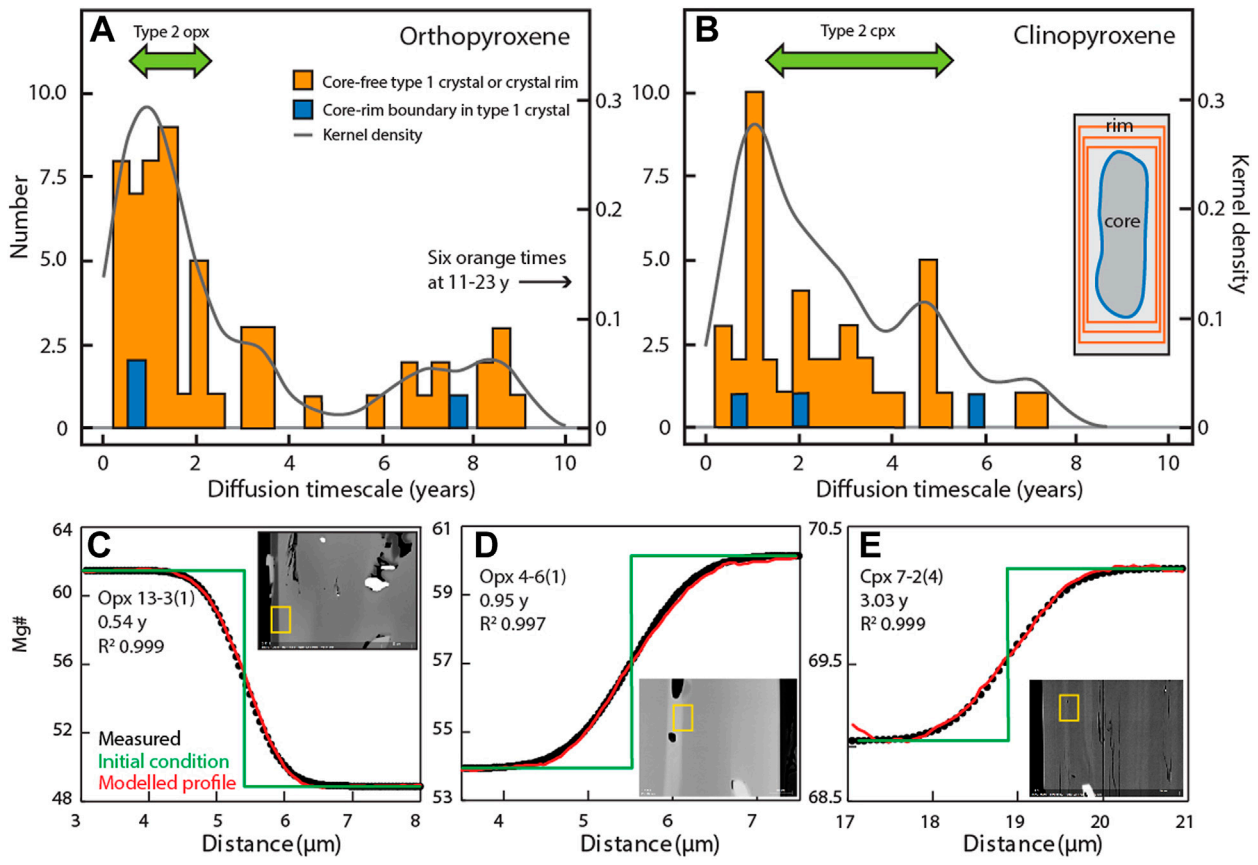

FIGURE 6
(A, B) Histograms of diffusion timescale estimates for opx and cpx in the PKP, with Gaussian kernel density curves (bandwidth 0.5; http://www.wessa.net/rwasp_density.wasp/). The blue data refer to the core-rim boundary of a type 1 crystal, the orange data refer to zone boundaries with the rims of cored type 1 crystals, or within core-free type 1 crystals. Green double arrows show the ranges of data for type 2 crystals. **(C–E)** Examples of diffusion models for the PKP. The Mg# (Mg number = 100 × Mg/[Mg+Fe] atomic) values for the measured profiles were calculated from microprobe-calibrated BSE images.

Modelling of Mg diffusion in a single, cored, type 1 plagioclase crystal gives a rim residence time at 905°C of no more than 5–10 years (Supplementary Material S1). This is consistent with the pyroxene results. It is also broadly consistent with the work of Zellmer et al. (1999) on Sr diffusion modelling in plagioclase crystals from several Kameni lavas (726, 1939–40, 1940 and 1950). Although some of Zellmer et al.'s crystals appeared to be sufficiently old for diffusive equilibrium to have been achieved, one had a residence timescale of ~100 years at 900°C.

7 Results for the M6 inter-Plinian eruptions and the Lower Pumice 2 caldera-forming eruption

Orthopyroxene crystals in the M6a and M6b pumice fall deposits have mutually similar compositional ranges ($Wo_{3-4}En_{62-68}Fs_{29-34}$) (Figure 7B). They are euhedral and generally weakly zoned, with 45–55 % exhibiting sector zoning and 15–25 % exhibiting a central line of melt inclusions indicative of initial skeletal growth followed by filling in to form prismatic shapes. Mg-Fe diffusion timescales were calculated for M6a for 49 compositional profiles in 12 crystals at the pre-eruptive temperature given by touching Fe-Ti oxides (Table 3). For M6b, 22 profiles were modelled in 15 crystals, assuming the same temperatures as for M6a, since ilmenite is absent in unit M6b. The two pumice fall deposits give short opx diffusion timescales: <0.01–10 years (mean 0.02 years) for M6a and 0.05–1 year (mean 0.1 years) for M6b (Figure 8).

The opx crystals in pumices of Lower Pumice 2 have a broader compositional range ($Wo_3En_{46-62}Fs_{35-51}$) than those in M6a and M6b, with stronger and more complex zoning (Figure 7A). In particular, about half of the crystals exhibit 'streaky' zoning due to prolonged Mg-Fe diffusion parallel to the crystal c axis around melt or mineral inclusions (Figure 3C) (Allan et al., 2013). Opx crystals in Lower Pumice 2 are also relatively rich in inclusions of Fe-Ti oxides and apatite. Crystals with sector zoning or phantom skeletal morphologies account for only 5–10 % of the opx, much smaller than in M6a and M6b. Mg-Fe diffusion timescales were determined on 9 crystals (13 profiles) at 856°C ± 16°C given by touching oxide pairs in the groundmass glass. The timescales are much longer than in Kameni, M6a or M6b, ranging from 10 to 1,000 years, with a mean of 400 years (Figure 8).

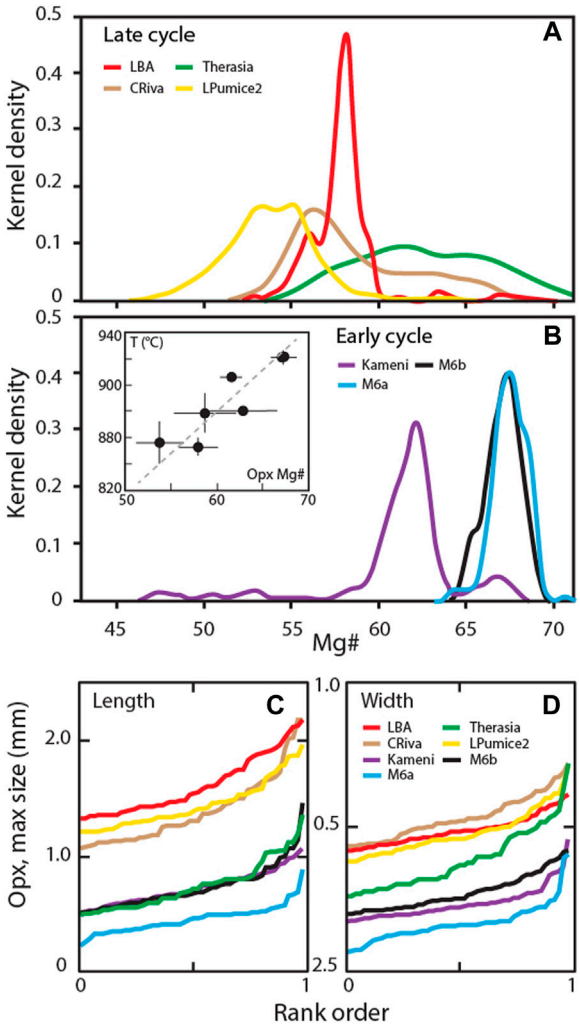

FIGURE 7
(A,B) Distributions of Mg# (Mg number = 100 × Mg/[Mg+Fe] atomic) of opx in **(A)** the four late-cycle eruptions, and **(B)** the three early-cycle eruptions using Gaussian kernel density curves (bandwidth 0; http://www.wessa.net/rwasp_density.wasp/) based on 100–530 analyses per eruption. The inset shows the correlation between opx Mg Number and eruption temperature calculated from co-existing Fe-Ti oxides. **(C,D)** Rank-ordered measurements of the sizes of the largest 50 opx crystals observed in the products of the seven eruptions, distinguishing between **(C)** length and **(D)** width.

8 Discussion

8.1 The Palaea Kameni Pumice eruption

To summarise, the PKP pumices contain two assemblages of macroscopic crystals.

Crystal assemblage 1 accounts for the large majority (85–95 %) of the crystals. It consists of opx (Mg# 58–68), cpx (Mg# 64–71) and plagioclase (An_{39-55}) with euhedral rims of Mg# 63–65, Mg# 67–69 and An_{48}, respectively, in glass with 70 wt% SiO_2. The opx and the cpx are observed in planar contact in crystal clusters, confirming that they belong to a single assemblage. Reference to phase equilibria experiments on Santorini magmas (Andújar et al., 2016) shows that the edge compositions form an equilibrium assemblage in ~70 wt% SiO_2 melt at 900°C–950°C and 4-6 wt% H_2O, consistent with the measured Fe-Ti oxide temperatures (905°C–926°C) and melt inclusion H_2O contents (4.1–5.2 wt%). Moreover, the range of interior compositions can be explained by cycling of the crystals through melts ranging from about 66 to 72 wt% SiO_2. Assemblage 1 crystals are therefore interpreted as autocrysts, i.e., they crystallized from the host melt or from silicic melts similar to it. Weak oscillatory and sawtooth zoning in these crystals probably record cycling in temperature, melt composition and/or H_2O pressure during growth (Ginibre et al., 2002; Streck, 2008). The sector zoned opx crystals grew rapidly, probably in skeletal form before filling in to form euhedral prisms. Crystallization of the

TABLE 3 Comparison of features of early-cycle and late-cycle eruptions.

Eruption	Early/late	Volume	Glass SiO_2	Mafic	Temp	H_2O MI[b]	CO_2 MI[b]	Opx	Opx	Opx	Timescale	Timescale
		km^3[a]	wt%	Enclaves?	°C	wt%	ppm	Sec zoned (%)	Central MI (%)	Streaky (%)	Range (y)	Mean (y)
Late Bronze Age	Late	32	73	Yes	853 ± 7	4.0–6.9	<50–200	47	13	32	1 to 1,000	30
Cape Riva	Late	39	70	Yes	879 ± 15	3.3–5.2	130–220	13	12	24	10 to 5,000	500
Lower Pumice 2	Late	12	72	Yes	856 ± 16	4.7–5.2	50–220	2	6	44	10 to 1,000	400
Therasia	Late	~0.2	(70)	Yes	(880)	ndet	ndet	5	9	25	10 to 4,000	400
Kameni PKP	Early	~0.1	70	Yes	906 ± 3	4.1–5.2	<50–140	23	24	2	0.1–10	2
M6b	Early	~0.1	68	?	921 ± 5	3.0–3.2	120–165	46	18	6	0.05–1	0.1
M6a	Early	~0.1	65	?	(921)	ndet	ndet	54	25	4	<0.01–10	0.02

ndet, not determined.

[a]See Table 1 for data sources.

[b]Melt inclusion (MI) volatile contents from Druitt et al. (2016).

autocrystic opx, cpx, and plag began a couple of decades prior to eruption, and was still ongoing a few months prior to eruption. It took place in the shallow magma reservoir at a depth of 4.3–6.0 km (based on melt inclusion volatile content), which corresponds to both the Kameni magma reservoir imaged by seismic tomography (McVey et al., 2020), and the uplift pressure source during unrest in 2011–12 (Parks et al., 2012; 2015). The corroded cores that occur in some type 1 crystals (Figure 4), may be antecrysts or xenocrysts overgrown by the autocrystic rims.

Crystal assemblage 2 (5–15 %) consists of opx (Mg# 48–60), cpx (Mg#58–60) and plagioclase (An_{26-34}) in glass with 70–72.5 wt% SiO_2. Some type 2 opx grew skeletally, like some type 1 opx, because they have central lines of melt inclusions. Some of the type-2 opx and cpx crystals also grew rapidly on timescales of a few years or less prior to eruption (Figure 6).

The crystal assemblages record at least two events of magma mixing prior to eruption. First, cores in some type 1 opx, cpx and plagioclase crystals are similar in composition to type 2 crystals (Figure 4). This suggests that mixing of two silicic magmas (one of which contained crystal assemblage 2) preceded growth of the type 1 crystals. Second, the two crystal assemblages and their melts were actively mingling immediately prior to eruption, because (1) the type 2 plagioclase crystals were actively reacting with the host melt, and (2) the melt was compositionally heterogeneous.

We now consider the implications of these data for the processes that led up to the PKP eruption. In so doing, we make the assumption that the PKP was preceded by processes similar to those of the other historical eruptions, and take into account other published observations for the Kameni system in general. First, the Kameni magmas are all dacitic, like the PKP (Barton and Huijsmans, 1986; Higgins et al., 2021). Second, most Kameni dacites contain quenched mafic enclaves (Martin et al., 2006), as does the PKP. Third, rare gas isotopic signatures associated with the unrest in 2011–12 can be explained by the injection of gas-charged mantle-derived basalt (Rizzo et al., 2015). There are two models for the Kameni system.

Model 1. It has been proposed that the eruptions and unrest periods of Kameni Volcano are triggered by the recharge of a long-lived, shallow, silicic reservoir by mafic magma (Barton and Huijsmans, 1986; Martin et al., 2006). The common presence of mafic enclaves in the dacitic products, as well as the rare gas isotopic signatures associated with unrest in 2011–12, both support this model (Rizzo et al., 2015). A problem, however, is that Model 1 does not readily explain the crystallisation event that preceded the PKP. The timescale of this crystallisation event is very short compared to the several centuries of dormancy that, to the best of our knowledge, preceded the eruption (from 46 CE to 726 CE). Crystallisation in hydrous silicic melts can be driven by (1) cooling, (2) decompression (Waters et al., 2015), (3) flushing by CO_2 released underplated mafic magmas (Caricchi et al., 2018), or (4) mixing with a cooler silicic magma (Druitt et al., 2012). In Model 1, intrusion of CO_2-rich basalt into a dacitic chamber could conceivably have caused a crystallisation event by lowering the H_2O activity in the silicic melt. However, the paucity of CO_2 (<140 ppm) in melt inclusions hosted in type 1 plagioclase in the PKP offers no evidence for this. A convincing explanation of the crystallisation event is therefore not offered by Model 1.

Model 2. Another possibility is that Kameni eruptions and unrest periods are preceded by the injection of mainly *silicic* magma into the

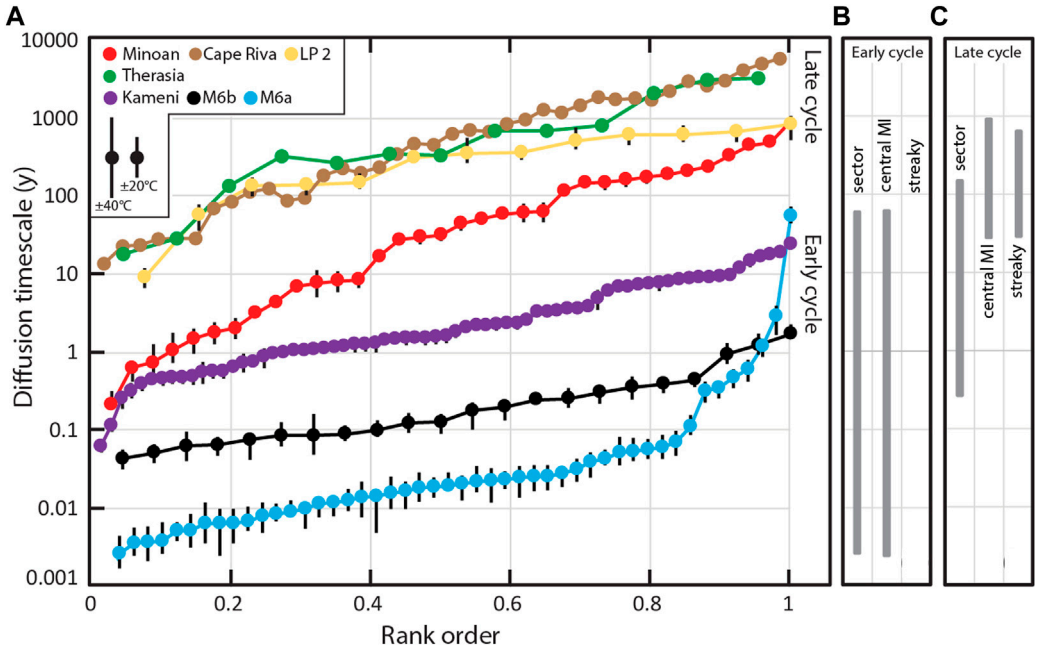

FIGURE 8
(A) Rank-ordered spectra of opx Mg-Fe diffusion timescales in the seven different eruptions. The uncertainties attached to each data point are based on minimum and maximum best fits. Black bars show the effects of temperature ranges on the timescale estimates. **(B, C)** The ranges of timescales given by crystals with certain distinctive textural features (sector zoning, central line of melt inclusions, inclusion-associated streaky zoning). 'Minoan' is another name for the Late Bronze Age (LBA) eruption.

shallow (4.3–6.0 km) reservoir (Parks et al., 2012). Mafic magma must also be injected, accounting for the mafic enclaves and rare gas signature, but the main injection batch is silicic. Model 2 is consistent with phase equilibria experimental studies that suggest that Kameni silicic melts are generated by fractional crystallisation in the lower to middle crust, then injected up into the upper crust (Andújar et al., 2015; see below). In Model 2, rapid crystal growth in the hydrous silicic melt could take place due to decompression and cooling during ascent and injection into the shallow reservoir (Waters et al., 2015). Mixing of silicic magmas of different compositions and crystal populations during transfer and injection would also drive crystal growth in the slightly hotter magma. One possibility is that the shallow reservoir contained a slightly more evolved, residual silicic melt (containing crystal assemblage 2) that mixed into the recharge silicic melt (causing crystallization of crystal assemblage 1). Another is that the two silicic melts (plus entrained mafic enclaves) ascended from depth and injected into the shallow reservoir together, both crystallising and mixing as they went. In Model 2, silicic recharge of the shallow reservoir started about 2 decades before the PKP eruption; it accelerated with time, with half the melt entering in the final few years, and was still ongoing immediately prior to eruption. We favour this model because it explains one or more crystallization events only decades to years prior to eruption.

8.2 Integration of the dataset

We now integrate our opx Mg-Fe diffusion results with those from previous papers on Santorini. The eruptions studied previously are the Cape Riva (22 ka; 39 km^3 DRE) and Late Bronze Age (3.6 ka, 32 km^3 DRE) caldera-forming eruptions, and three flows of the ~0.2 km^3 Therasia silicic lavas that leaked out a few thousand years prior to the Cape Riva eruption (Table 1) (Fabbro et al., 2017; Flaherty et al., 2018). The volumes for Cape Riva and LBA are estimates based on a new study of deep-sea tephra from Santorini (Kutterolf et al., 2021). In integrating the opx datasets, we have recalculated the diffusion timescales of Fabbro et al. (2017) using the a-axis Dohmen et al. (2016) diffusion coefficient, so as to be consistent with those of Flaherty et al. (2018) and the present study. The features of the eruptions from the present and previous studies are compared in Table 3. Population density plots of opx compositions are compared in Figures 7A,B, and opx crystal sizes are compared in Figures 7C,D. The opx timescales are presented, rank-ordered, in Figure 8.

8.3 Big eruptions on Santorini are small eruptions made big

Our study of the ~0.1 km^3 PKP allows us to compare it petrologically with the 39 km^3 Cape Riva and 32 km^3 LBA caldera-forming eruptions (Kutterolf et al., 2021), which were studied to a similar level of detail. Apart from the large volume difference, the products show several similarities (Table 3): (1) all contain 5–20 % crystals, (2) all contain plagioclase crystals with antecrystic/xenocrystic cores and distinct autocrystic rims, (3) all contain opx crystals that are sector zoned, with or without phantom skeletal morphologies, (4) all contain evidence for the mingling of compositionally variable silicic melts, (5) the mineral phases in all

three eruptions yield crystal diffusion timescales (Mg-Fe in opx and cpx; Mg in plagioclase) that are much shorter than the duration of the preceding repose period, and (6) all contain mafic enclaves showing the involvement of mafic magma in the eruption. Our opx data for the ~0.1 km^3 M6a and M6b eruptions and the 12 km^3 Lower Pumice 2 caldera-forming eruption reinforce these similarities, since points 1, 3, 5 and 6 (LP2 only) also apply to them. Despite volumes more than two orders of magnitude greater, the large silicic eruptions appear to be preceded by processes of storage and recharge similar to those of the small silicic eruptions, but on a larger scale. Big eruptions on Santorini are small eruptions made big.

There are also differences, however, notably between the small (~0.1 km^3) early-cycle (M6a, M6b, Kameni) and large (10–40 km^3) late-cycle (LP2, CR, LBA) eruptions. Relative to the small eruptions, opx crystals in the large eruptions have (1) larger sizes (Figures 7C,D), (2) larger compositional ranges (Figures 7A,B), (3) a significant (yet still minor) proportion of strongly or complexly (resorbed, sieved) zoned crystals, (4) larger proportions of streaky-zoned opx crystals, and (5) opx diffusion timescales that are systematically longer (1–5,000 years in large eruptions; <0.01–10 years in small eruptions) (Figure 8). The larger crystal sizes and streaky-zoned crystals (all of which give diffusion times of 30 years or more) are consistent with longer crystal residence prior to the large eruptions, and the larger compositional ranges and presence of non-simple crystal textures are consistent with more complex pre-eruptive magma histories. Sector zoned or skeletal opx crystals give widely varying diffusion timescales, from <0.01 years in the small eruptions up to as much as 850 years in the large eruptions (Figure 8), showing that all eruptions contain opx crystals that grew rapidly, then resided for different lengths of time in the magma.

The late-cycle Therasia lavas are, however, an exception. Despite their small volumes (~0.2 km^3), they have opx crystals with large compositional ranges, common streaky zoning, and sizes intermediate between those of the other two groups. Furthermore, their diffusion timescales are similar to those of the end-cycle eruptions, in particular the Cape Riva eruption that followed them by just a few thousand years. Although the Therasia samples are lavas, the long opx timescales are believed to record pre-eruptive processes, not the post-eruptive cooling of the lava, because the centre of even a 50-m-thick silicic lava will cool by 400°C–500°C in only 30 years (Manley, 1992). These small, late-cycle magma leaks share the long pre-eruptive opx residence of an end-cycle caldera-forming eruption.

8.4 Opx diffusion timescales do not correlate with eruption volume, but with position in a caldera cycle

There have been few studies to date of whether and how crystal diffusion timescales vary with eruption magnitude. Costa (2008) compiled crystal residence times obtained using a range of techniques (including U-Th and U-Pb ages in zircon, Sr and Ba diffusion in sanidine, and Ti zoning in quartz) and plotted them against eruption volume. Although there was a hint that smaller eruptions were associated with shorter crystal residence, no clear correlation emerged. Ostorero et al. (2021) found that opx Mg-Fe diffusion timescales of two 4–5 km^3 silicic eruptions were longer than those of three eruptions an order of magnitude smaller in volume at Dominica Volcano (Antilles), and Mangler et al. (2022) found some differences in opx diffusion timescales between explosive and effusive eruptions of small volume at Popocatépetl (Mexico).

Our new data allow us to explore if such a correlation exists at Santorini. It is tested in Figure 9C, on which we plot opx diffusion timescale *versus* volume for our seven eruptions. While the Kameni, M6a, M6b, LP2 and CR data correlate positively with volume, the Therasia lavas have timescales that are too high, and the LBA eruption timescales that are too low for their respective volumes. The scatter rules out any strong correlation of crystal diffusion time and eruption volume at Santorini, and suggests that other factors are at play.

Another possibility is that diffusion time correlates not with eruptive volume, but with magmatic stage during the development of a caldera cycle. Costa (2008) tested this hypothesis for his data, and found that crystals in even small eruptions during the build-up to caldera-forming eruptions at Long Valley, Taupo and Yellowstone had residence times comparable to those of the caldera-forming eruptions themselves. This suggested that the pre-caldera magmas derived from the same magma reservoir as the caldera-forming magma. Crystals from at least some post-caldera eruptions, however, had residence times that were short compared to the caldera-forming eruption, suggesting the presence of new magma and crystal batches following caldera collapse.

Re-evaluating our Santorini data in this context, we find that our crystal diffusion timescales indeed separate clearly into two groups if considered on the basis of position within a caldera cycle (Figure 9B). Eruptions M6a, M6b and Kameni occur early in their respective cycles and have opx timescales of <0.01–10 years, while LP2, Th, CR, and LBA occur late in their respective cycles and have timescales in the range 1–5,000 years. The Therasia lavas have long opx diffusion timescales because they were discharged very late in a caldera cycle.

8.5 Recharge timescales and caldera cycles

Our data can be understood in terms of the existing model for the Santorini transcrustal magmatic system (Cottrell et al., 1999; Cadoux et al., 2014; Andújar et al., 2015; Andújar et al., 2016; Flaherty et al., 2018) and for caldera systems in general (Bouvet de Maisonneuve et al., 2021). Silicic melts at Santorini are believed to be generated in gabbroic or dioritic mushes in the lower to middle crust, then transferred to an upper crustal holding chamber, situated at depths between 4 and 8 km, prior to eruption. We refer to these respectively as the deep and shallow magma reservoirs, while recognizing that the real architecture is more complex (Figure 10A).

Our previous studies of the 3.6 ka LBA and 22 ka Cape Riva caldera-forming eruptions showed that crystals grow in the hydrous silicic melts during transfer from the deep to shallow reservoirs due to a combination of decompression, cooling, and magma mixing (Druitt et al., 2012; 2016; Fabbro et al., 2017; Flaherty et al., 2018) (Figure 10B). These crystals then reside in the shallow reservoir until quenched by eruption. We interpreted the diffusion timescales given

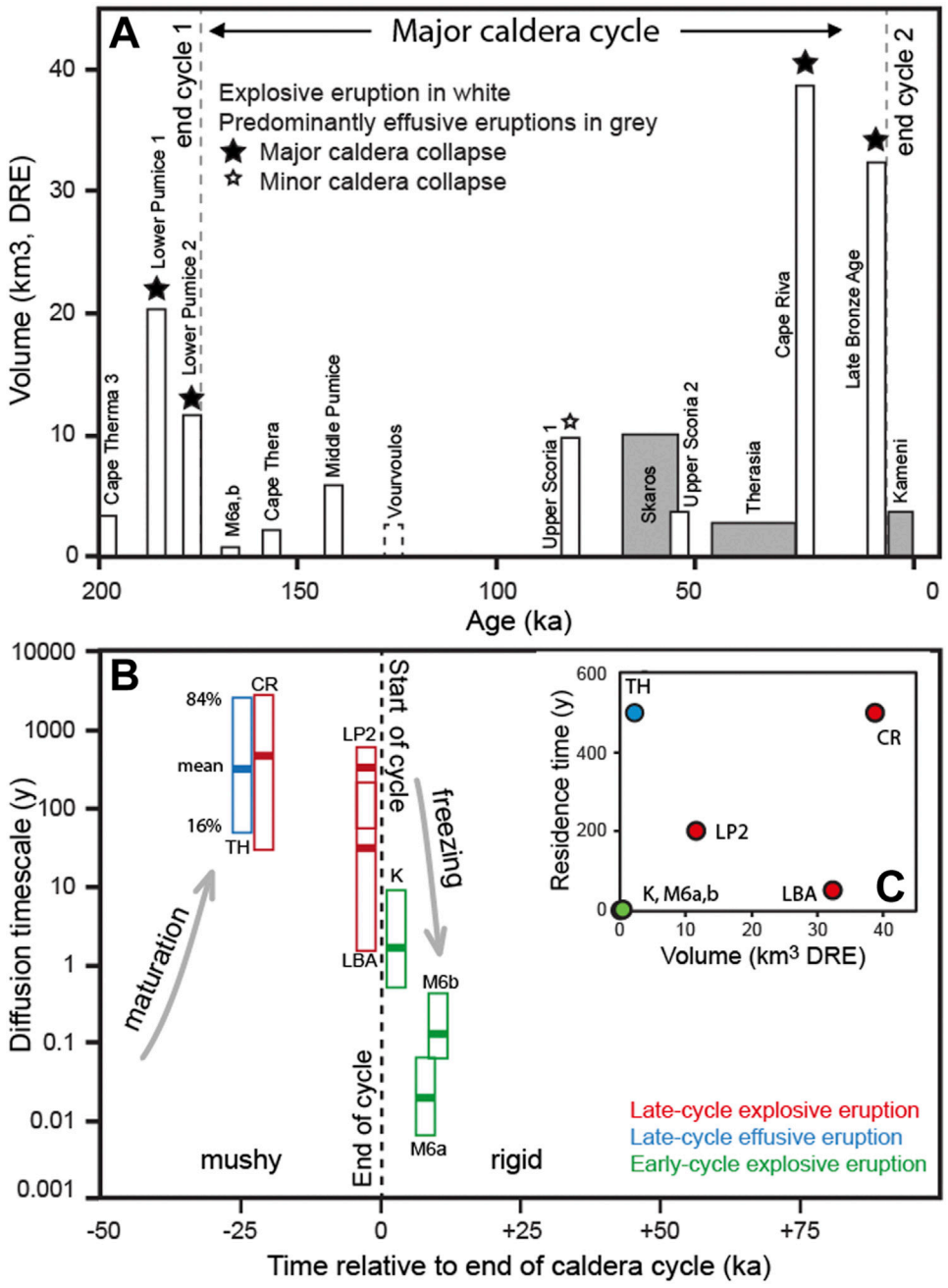

FIGURE 9
(A) Plot of eruption DRE (dense rock equivalent) volume vs. age for the last 2005 ka at Santorini. The volume estimates are minima based on the volumes of deep-sea ashes (Kutterolf et al., 2021). The volumes for the Skaros and Therasia lavas are from Druitt et al. (1999). Explosive eruptions are in white, and predominantly effusive eruptions are in grey. Caldera cycle 2 began following the 1775 ka Lower Pumice 2 eruption and ended with the 3.6 ka Late Bronze-Age eruption. **(B)** Mean opx diffusion timescale for the seven eruptions showing the higher values for the late-cycle eruptions, including the Therasia lavas. The data are arranged temporally relative to the end of a caldera cycle, so that the data for cycles 1 and 2 are shown together. **(C)** The inset shows the lack of any straightforward correlation of opx crystal diffusion time with eruption volume.

by Mg-Fe in pyroxenes and Mg in plagioclase as the time between pre-eruptive recharge of the shallow reservoir (by a particular magma batch) and eruption: the recharge timescale. On this basis, we concluded that caldera-forming eruptions are preceded by processes occurring on three very different timescales (Cottrell et al., 1999; Druitt et al., 2012; Parks et al., 2012; Flaherty et al., 2018): (1) silicic melts are generated in the deep mush reservoir and segregated into melt-rich lenses (10^3–10^4 years); (2) one or more rapid events of mush reorganization result in short lived, high-flux transfer of the melts (± entrained mafic enclaves) to the shallow reservoir ($<10^2$–10^3 years prior to eruption); (3) the eruption is triggered.

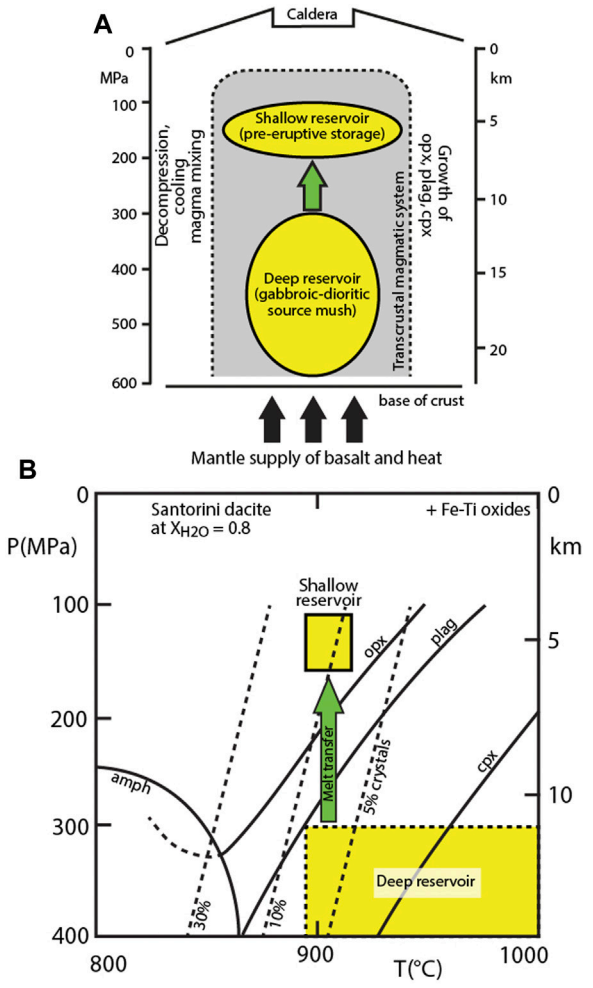

FIGURE 10
(A) Sketch of the transcrustal magmatic system beneath Santorini, based on the phase equilibria data of Cadoux et al. (2014); Andújar et al. (2016), and the melt inclusion volatile barometry data of Druitt et al. (2016). Silicic melts are believed to be generated in gabbroic/dioritic mushes in the mid-to-lower crust (deep reservoir), then extracted and transferred to an upper crustal storage level (shallow reservoir) prior to either eruption or plutonic death. Decompression, cooling and mixing of silicic magma batches during melt transfer is believed to drive crystallization of opx, cpx and plagioclase, either as new crystals or as rims on pre-existing crystals. **(B)** Phase diagram for Santorini dacitic magma, based on the mixed-volatile experiments of Cadoux et al. (2014). The shallow reservoir shown is that for the PKP, from Druitt et al. (2016); McVey et al. (2020). The phase diagram shows that melt transfer (green arrow) from the mid-to-lower crustal source region (deep reservoir), to the pre-eruptive storage level (shallow reservoir) will result in crystallization of opx, cpx and plagioclase (±oxides) due to lowering of pressure; any cooling or mixing with resident cooler magmas will have the same effect.

Given the petrological similarity of small and large eruptions at Santorini, as discussed above, we now extend this model to small eruptions such as those of Kameni and the M6 inter-Plinian period. Model 2 for Kameni explains the crystal features and short diffusion timescales of the PKP better than Model 1, and is consistent with interpretation of the larger eruptions.

The relationship between reservoir recharge timescale and position in the caldera cycle may reflect temporal changes in the mechanical response of the shallow reservoir to inputs of magma from below (Annen et al., 2006; Gelman et al., 2013; Caricchi et al., 2014; Degruyter and Huber, 2014; Degruyter et al., 2016; Karakas et al., 2017; Sparks et al., 2019; Townsend et al., 2019). During the early stages of a caldera cycle there is little melt in the shallow reservoir, which therefore behaves rigidly. Batches of silicic (±mafic) melt and gas arriving in the shallow reservoir therefore rapidly build up overpressure and erupt once the fracture limit is exceeded and a dyke capable of reaching the surface is created. Early-cycle silicic melt batches (right of time zero on Figure 9B) therefore contain opx populations that are young and texturally simple. Melt batches that do not erupt then cool and solidify at the storage level (e.g., the intrusions that caused the caldera unrest of 2011–12; Parks et al., 2012).

As the caldera cycle advances, the melt fraction in the reservoir increases due to thermal maturation, sustained H_2O fluxing, and defrosting of plutonic rocks and mushes containing low-temperature or hydrous mineral phases. Pulses of melt supply to the shallow reservoir are now accommodated by the viscoelastic response of the surrounding reservoir (Jellinek and DePaolo, 2003), aided by lateral sill propagation and by floor subsidence due to compaction of the underlying mushes (Sparks et al., 2019). The presence of a free volatile phase would increase melt compressibility, making the reservoir harder to pressurize and thus decreasing the likelihood of eruptions (Caricchi et al., 2014; Degruyter and Huber, 2014; Townsend et al., 2019). These effects counteract pressure accumulation in the shallow reservoir, allowing for larger volumes of melt to accumulate than earlier in the caldera cycle. Sustained, accelerating, silicic recharge can therefore last several centuries or millennia before conditions are reached to trigger a caldera-forming eruption (left of time zero on Figure 9B). During these long periods of melt accumulation in the shallow reservoir, opx crystals grow larger, diffusion profiles broaden, and relatively rapid diffusion parallel to the crystal c axis generates streaky zoning adjacent to mineral and melt inclusions. Small leaks of late-cycle silicic magma preceding caldera-forming eruptions (like the Therasia lavas) also record these long-residence conditions. Finally, some combination of overpressure, roof instability, volatile exsolution or tectonic forcing triggers the caldera-forming eruption. Large-scale melt decompression and outgassing during caldera collapse then takes place, causing extensive crystallization of remaining melt in the magmatic system, rigidifying the subvolcanic crust and starting a new cycle (Klemetti et al., 2011; Bachmann et al., 2012).

9 Conclusion

This study was conceived to address two questions related to the Santorini magmatic system. The answers are as follows.

Are the processes leading up to small eruptions the same as in large eruptions? Similarities in the petrological features of crystal cargoes lead us to conclude that this is probably the case. All contain 5–20 % crystals, plagioclase crystals with antecrystic/xenocrystic cores and distinct autocrystic rims, sector-zoned opx with or without phantom skeletal morphologies, and mean opx Mg-Fe diffusion timescales of less than 500 years. Some have evidence for the mingling of compositionally distinct silicic melts and/or

contain mafic enclaves from mingling with mafic magma. Based on previous studies of phase equilibria, crystal hosted melt inclusions, and petrological studies of large Santorini eruptions, autocrystic crystals are believed to grow (driven by decompression, cooling, magma mixing) during the ascent of hydrous silicic melts from a deep mush reservoir to an upper crustal holding chamber prior to eruption. Consequently, crystal diffusion times are interpreted as a measure of recharge timescale: the time between recharge of the shallow reservoir and eruption. We propose that the same processes precede small eruptions at Santorini, on a smaller scale.

How do recharge timescales vary with eruption magnitude and throughout a caldera cycle? Recharge timescales do not correlate with eruption magnitude (from ~0.1 to 40 km^3 DRE), but vary systematically with different stages of a caldera cycle. Integration of the opx Mg-Fe diffusion timescales from seven Santorini eruptions shows that they increase through each 180 ka caldera cycle, being less than a few years during the early stages of the cycle, and up to a few centuries or millennia towards the end. We attribute this increase to thermal maturation and H_2O-flushing of the transcrustal magma system from the start to finish of a cycle, causing the system to change its mechanical response to melt inputs from rigid to mushy. This allows accumulation of progressively larger layers in the upper crustal reservoir as the caldera cycle progresses. Sustained silicic recharge of the reservoir late in a caldera cycle can last several centuries or millennia before conditions are reached to trigger a caldera-forming eruption.

The data and interpretations presented in this paper need to be tested and extended both at Santorini and at other caldera systems. We recommend that time series studies of opx diffusion timescales in erupted products be integrated into hazards assessments at restless calderas (Re et al., 2021).

Data availability statement

The original contributions presented in the study are included in the article/Supplementary Material, further inquiries can be directed to the corresponding author.

Author contributions

TD and PN collected the samples. AP-S studied the pyroxenes of the PKP, and TF studied those of the Lower Pumice 2 and two M6 eruptions. GH studied the plagioclase of the PKP. GF and TF provided pyroxene data from previous studies. HB-B obtained the funding for the study. TD oversaw the project and wrote the first draft of the manuscript, which was then discussed and edited by HB-B and the other authors. All authors contributed to the article and approved the submitted version.

Funding

The project was funded by the French Agence National de Recherche project V-CARE (ANR-18-CE03-0010). AP-S acknowledges his grant "Programa Propio III Universidad de Salamanca 2021 co-funded by Banco de Santander". Banco de Santander was not involved in the study design, collection, analysis, interpretation of data, the writing of this article, or the decision to submit it for publication.

Acknowledgments

Jean-Luc Devidal and Emmy Voyer provided mineral analyses and imagery, and Nicolas Cluzel and Claire Fonquernie offered technical assistance. We thank Chiara Petrone and Eugenio Nicotra for their helpful comments. We are very grateful to Georges Boudon in his coordination of the V-CARE project. This is Laboratory of Excellence ClerVolc contribution 603.

Conflict of interest

The authors declare that the research was conducted in the absence of any commercial or financial relationships that could be construed as a potential conflict of interest.

Publisher's note

Supplementary material

The Supplementary Material for this article can be found online at: https://www.frontiersin.org/articles/10.3389/feart.2023.1128083/full#supplementary-material

References

Acocella, V., Di Lorenzo, R., Newhall, C., and Scandone, R. (2015). An overview of recent (1988 to 2014) caldera unrest: Knowledge and perspectives. *Rev. Geophys.* 53, 896–955. doi:10.1002/2015RG000492

Allan, A. S. R., Morgan, D. J., Wilson, C. J. N., and Millet, M. A. (2013). From mush to eruption in centuries: Assembly of the super-sized oruanui magma body. *Contrib. Mineral. Pet.* 166, 143–164. doi:10.1007/s00410-013-0869-2

Allan, A., Barker, S. J., Millet, M. A., Morgan, D. J., Rooyakkers, S. M., Schipper, C. I., et al. (2017). A cascade of magmatic events during the assembly and eruption of a super-sized magma body. *Contrib. Mineral. Pet.* 172 (7), 49–34. doi:10.1007/s00410-017-1367-8

Andersen, D. J., and Lindsley, D. H. (1988). Internally consistent solution models for Fe-Mg-Mn-Ti oxides; Fe-Ti oxides. *Am. Mineral.* 73 (7-8), 714–726.

Andújar, J., Scaillet, B., Pichavant, M., and Druitt, T. H. (2015). Differentiation conditions of a basaltic magma from Santorini, and its bearing on the production of andesite in arc settings. *J. Petrol.* 56 (4), 765–794. doi:10.1093/petrology/egv016

Andújar, J., Scaillet, B., Pichavant, M., and Druitt, T. H. (2016). Generation conditions of dacite and rhyodacite via the crystallization of an andesitic magma. Implications for the plumbing system at santorini (Greece) and the origin of tholeiitic or calc-alkaline differentiation trends in arc magmas. *J. Petrol.* 57 (10), 1887–1920. doi:10.1093/petrology/egw061

Annen, C., Blundy, J. D., and Sparks, R. S. J. (2006). The Genesis of intermediate and silicic magmas in deep crustal hot zones. *J. Petrol.* 47 (3), 505–539. doi:10.1093/petrology/egi084

Bachmann, O., and Huber, C. (2016). Silicic magma reservoirs in the Earth's crust. *Am. Mineral.* 101 (11), 2377–2404. doi:10.2138/am-2016-5675

Bachmann, O., and Huber, C. (2019). The inner workings of crustal distillation columns; the physical mechanisms and rates controlling phase separation in silicic magma reservoirs. *J. Petrol.* 60 (1), 3–18. doi:10.1093/petrology/egy103

Bachmann, O., Deering, C. D., Ruprecht, J. S., Huber, C., Skopelitis, A., and Schnyder, C. (2012). Evolution of silicic magmas in the kos-nisyros volcanic center, Greece: A petrological cycle associated with caldera collapse. *Contrib. Mineral. Pet.* 163 (1), 151–166. doi:10.1007/s00410-011-0663-y

Balcone-Boissard, H., Boudon, G., Blundy, J. D., Martel, C., Brooker, R. A., Deloule, E., et al. (2018). Deep pre-eruptive storage of silicic magmas feeding Plinian and dome-forming eruptions of central and northern Dominica (Lesser Antilles) inferred from volatile contents of melt inclusions. *Contrib. Mineral. Pet.* 173 (12), 101–124. doi:10.1007/s00410-018-1528-4

Barker, S. J., Wilson, C. J., Morgan, D. J., and Rowland, J. V. (2016). Rapid priming, accumulation, and recharge of magma driving recent eruptions at a hyperactive caldera volcano. *Geology* 44 (4), 323–326. doi:10.1130/G37382.1

Barton, M., and Huijsmans, J. P. P. (1986). Post-caldera dacites from the santorini volcanic complex, aegean sea, Greece: An example of the eruption of lavas of near-constant composition over a 2,200 year period. *Contrib. Mineral. Pet.* 94 (4), 472–495. doi:10.1007/BF00376340

Bergantz, G. W., Schleicher, J. M., and Burgisser, A. (2015). Open-system dynamics and mixing in magma mushes. *Nat. Geosci.* 8, 793–796. doi:10.1038/ngeo2534

Bouvet de Maisonneuve, C., Forni, F., and Bachmann, O. (2021). Magma reservoir evolution during the build up to and recovery from caldera-forming eruptions – a generalizable model? *Earth-Science Rev.* 218, 103684. doi:10.1016/j.earscirev.2021.103684

Brugman, K., Till, C. B., and Bose, M. (2022). Common assumptions and methods yield overestimated diffusive timescales, as exemplified in a Yellowstone post - caldera lava. *Contrib. Mineral. Pet.* 177 (6), 63–19. doi:10.1007/s00410-022-01926-5

Cadoux, A., Scaillet, B., Druitt, T. H., and Deloule, E. (2014). Magma storage conditions of large plinian eruptions of santorini volcano (Greece). *J. Petrol.* 55 (6), 1129–1171. doi:10.1093/petrology/egu021

Caricchi, L., Annen, C., Blundy, J., Simpson, G., and Pinel, V. (2014). Frequency and magnitude of volcanic eruptions controlled by magma injection and buoyancy. *Nat. Geosci.* 7 (2), 126–130. doi:10.1038/ngeo2041

Caricchi, L., Sheldrake, T. E., and Blundy, J. (2018). Modulation of magmatic processes by CO_2 flushing. *Earth Planet. Sci. Lett.* 491, 160–171. doi:10.1016/j.epsl.2018.03.042

Cashman, K., and Blundy, J. (2013). Petrological cannibalism: The chemical and textural consequences of incremental magma body growth. *Contrib. Mineral. Pet.* 166 (3), 703–729. doi:10.1007/s00410-013-0895-0

Cashman, K. V., Sparks, R. S. J., and Blundy, J. D. (2017). Vertically extensive and unstable magmatic systems: A unified view of igneous processes. *Science* 355, eaag3055. doi:10.1126/science.aag3055

Chamberlain, K. J., Morgan, D. J., and Wilson, C. J. (2014). Timescales of mixing and mobilisation in the bishop tuff magma body: Perspectives from diffusion chronometry. *Contrib. Mineral. Pet.* 168 (1), 1034–1124. doi:10.1007/s00410-014-1034-2

Cole, J. W., Milner, D. M., and Spinks, K. D. (2005). Calderas and caldera structures: A review. *Earth-Science Rev.* 69 (1-2), 1–26. doi:10.1016/j.earscirev.2004.06.004

Cooper, K. M., and Kent, A. J. R. (2014). Rapid remobilization of magmatic crystals kept in cold storage. *Nature* 506, 480–483. doi:10.1038/nature12991

Costa, F., Chakraborty, S., and Dohmen, R. (2003). Diffusion coupling between trace and major elements and a model for calculation of magma residence times using plagioclase. *Geochim. Cosmochim. Acta* 67 (12), 2189–2200. doi:10.1016/S0016-7037(02)01345-5

Costa, F., Dohmen, R., and Chakraborty, S. (2008). Time scales of magmatic processes from modeling the zoning patterns of crystals. *Rev. Mineral. Geochem.* 69 (1), 545–594. doi:10.2138/rmg.2008.69.14

Costa, F., Andreastuti, S., Bouvet de Maisonneuve, C., and Pallister, J. S. (2013). Petrological insights into the storage conditions, and magmatic processes that yielded the centennial 2010 Merapi explosive eruption. *J. Volcanol. Geotherm. Res.* 261, 209–235. doi:10.1016/j.jvolgeores.2012.12.025

Costa, F., Shea, T., and Ubide, T. (2020). Diffusion chronometry and the timescales of magmatic processes. *Nat. Rev. Earth Environ.* 1 (4), 201–214. doi:10.1038/s43017-020-0038-x

Costa, F. (2008). "Residence times of silicic magmas associated with calderas," in *Caldera volcanism: Analysis, modelling and response. Developments in Volcanology*. Editors J. Gottsmann and J. Martí (Elsevier), 10, 1–55. doi:10.1016/S1871-644X(07)00001-0

Cottrell, E., Gardner, J. E., and Rutherford, M. J. (1999). Petrologic and experimental evidence for the movement and heating of the pre-eruptive Minoan rhyodacite (Santorini, Greece). *Contrib. Mineral. Pet.* 135 (4), 315–331. doi:10.1007/s004100050514

de Silva, S., Salas, G., and Schubring, S. (2008). Triggering explosive eruptions: The case for silicic magma recharge at Huaynaputina, southern Peru. *Geol* 36 (5), 387–390. doi:10.1130/G24380A.1

Degruyter, W., and Huber, C. (2014). A model for eruption frequency of upper crustal silicic magma chambers. *Earth Planet. Sci. Lett.* 403, 117–130. doi:10.1016/j.epsl.2014.06.047

Degruyter, W., Huber, C., Bachmann, O., Cooper, K. M., and Kent, A. J. R. (2016). Magma reservoir response to transient recharge events: The case of santorini volcano (Greece). *Geology* 44, 23–26. doi:10.1130/G37333.1

Dohmen, R., Ter Heege, J. H., Becker, H. W., and Chakraborty, S. (2016). Fe-Mg interdiffusion in orthopyroxene. *Am. Mineral.* 101 (10), 2210–2221. doi:10.2138/am-2016-5815

Druitt, T. H., Edwards, L., Mellors, R. M., Pyle, D. M., Sparks, R. S. J., Lanphere, M., et al. (1999). "Santorini volcano," in *Geological society london memoir* (London: Cambridge University Press), 19. doi:10.1017/S0016756800224138

Druitt, T. H., Costa, F., Deloule, E., Dungan, M., and Scaillet, B. (2012). Decadal to monthly timescales of magma transfer and reservoir growth at a caldera volcano. *Nature* 482 (7383), 77–80. doi:10.1038/nature10706

Druitt, T. H., Mercier, M., Florentin, L., Deloule, E., Cluzel, N., Flaherty, T., et al. (2016). Magma storage and extraction associated with plinian and interplinian activity at Santorini Caldera (Greece). *J. Petrol.* 57 (3), 461–494. doi:10.1093/petrology/egw015

Druitt, T. H. (2014). New insights into the initiation and venting of the Bronze-Age eruption of Santorini (Greece), from component analysis. *Bull. Volcanol.* 76 (2), 794–821. doi:10.1007/s00445-014-0794-x

Elms, H. C., Barker, S. J., Morgan, D. J., Wilson, C. J., and Charlier, B. L. (2023). Processes and timescales of magmatic rejuvenation and residence prior to post-caldera rhyolitic eruptions: Ōkataina Volcanic Centre, Aotearoa New Zealand. *J. Volcanol. Geotherm. Res.* 437, 107790. doi:10.1016/j.jvolgeores.2023.107790

Fabbro, G. N., Druitt, T. H., and Costa, F. (2017). Storage and eruption of silicic magma across the transition from dominantly effusive to caldera-forming states at an arc volcano (Santorini, Greece). *J. Petrol.* 58 (12), 2429–2464. doi:10.1093/petrology/egy013

Flaherty, T., Druitt, T. H., Tuffen, H., Higgins, M. D., Costa, F., and Cadoux, A. (2018). Multiple timescale constraints for high-flux magma chamber assembly prior to the Late Bronze Age eruption of Santorini (Greece). *Contrib. Mineral. Pet.* 173 (9), 75–21. doi:10.1007/s00410-018-1490-1

Flaherty, T., Druitt, T. H., Francalanci, L., Schiano, P., and Sigmarsson, O. (2022). Temporal variations in the diversity of primitive melts supplied to the Santorini silicic magmatic system and links to lithospheric stresses. *Contrib. Mineral. Pet.* 177 (8), 79. doi:10.1007/s00410-022-01941-6

Fytikas, M., Kolios, N., and Vougioukalakis, G. (1990). "Post-Minoan activity of the Santorini volcano: Volcanic hazard and risk, forecasting possibilities," in *Thera and the aegean world III*. Editors D. A. Hardy, J. Keller, V. P. Galanopou-los, N. C. Flemming, and T. H. Druitt (London: The Thera Foundation), 2, 183–198.

Gelman, S. E., Gutíerrez, F. J., and Bachmann, O. (2013). On the longevity of large upper crustal silicic magma reservoirs. *Geol* 41 (7), 759–762. doi:10.1130/G34241.1

Ghiorso, M. S., and Evans, B. W. (2008). Thermodynamics of rhombohedral oxide solid solutions and a revision of the Fe-Ti two-oxide geothermometer and oxygen-barometer. *Am. J. Sci.* 308 (9), 957–1039. doi:10.2475/09.2008.01

Ginibre, C., Wörner, G., and Kronz, A. (2002). Minor-and trace-element zoning in plagioclase: Implications for magma chamber processes at parinacota volcano, northern Chile. *Contrib. Mineral. Pet.* 143 (3), 300–315. doi:10.1007/s00410-002-0351-z

Higgins, M. D., Debecq, A., Vander Auwera, J., and Nomikou, P. (2021). Chemical and textural diversity of Kameni (Greece) dacites: Role of vesiculation in juvenile and mature basal crystal masses. *Contrib. Mineral. Pet.* 176 (2), 13–20. doi:10.1007/s00410-020-01764-3

Hildreth, W. (2004). Volcanological perspectives on Long Valley, mammoth mountain, and mono craters: Several contiguous but discrete systems. *J. Volcanol. Geotherm. Res.* 136 (3-4), 169–198. doi:10.1016/j.jvolgeores.2004.05.019

Jellinek, A. M., and DePaolo, D. J. (2003). A model for the origin of large silicic magma chambers: Precursors of caldera-forming eruptions. *Bull. Volcanol.* 65 (5), 363–381. doi:10.1007/s00445-003-0277-y

Jenkins, S. F., Barsotti, S., Hincks, T. K., Neri, A., Phillips, J. C., Sparks, R. S. J., et al. (2015). Rapid emergency assessment of ash and gas hazard for future eruptions at Santorini Volcano, Greece. *J. Appl. Volcanol.* 4 (1), 16–22. doi:10.1186/s13617-015-0033-y

Karakas, O., Degruyter, W., Bachmann, O., and Dufek, J. (2017). Lifetime and size of shallow magma bodies controlled by crustal-scale magmatism. *Nat. Geosci.* 10, 446–450. doi:10.1038/ngeo2959

Kilgour, G. N., Saunders, K. E., Blundy, J. D., Cashman, K. V., Scott, B. J., and Miller, C. A. (2014). Timescales of magmatic processes at Ruapehu volcano from diffusion chronometry and their comparison to monitoring data. *J. Volcanol. Geotherm. Res.* 288, 62–75. doi:10.1016/j.jvolgeores.2014.09.010

Klemetti, E. W., Deering, C. D., Cooper, K. M., and Roeske, S. M. (2011). Magmatic perturbations in the Okataina Volcanic Complex, New Zealand at thousand-year

timescales recorded in single zircon crystals. *Earth Planet. Sci. Lett.* 305 (1-2), 185–194. doi:10.1016/j.epsl.2011.02.054

Konstantinou, K. I. (2010). Crustal rheology of the Santorini–Amorgos zone: Implications for the nucleation depth and rupture extent of the 9 July 1956 Amorgos earthquake, southern Aegean. *J. Geodyn.* 50 (5), 400–409. doi:10.1016/j.jog.2010.05.002

Koyaguchi, T., and Kaneko, K. (1999). A two-stage thermal evolution model of magmas in continental crust. *J. Petrol.* 40 (2), 241–254. doi:10.1093/petroj/40.2.241

Krimer, D., and Costa, F. (2017). Evaluation of the effects of 3D diffusion, crystal geometry, and initial conditions on retrieved time-scales from Fe–Mg zoning in natural oriented orthopyroxene crystals. *Geochim. Cosmochim. Acta* 196, 271–288. doi:10.1016/j.gca.2016.09.037

Kutterolf, S., Freundt, A., Druitt, T. H., Mcphie, J., Nomikou, P., Pank, K., et al. (2021). The medial offshore record of explosive volcanism along the central to eastern aegean Volcanic Arc: 2. Tephra ages and volumes, eruption magnitudes and marine sedimentation rate variations. *Geochem. Geophys. Geosyst.* 22 (12), e2021GC010011. doi:10.1029/2021GC010011

Lepage, L. D. (2003). Ilmat: An excel worksheet for ilmenite-magnetite geothermometry and geobarometry. *Comput. Geosci.* 29 (5), 673–678. doi:10.1016/S0098-3004(03)00042-6

Mangler, M. F., Petrone, C. M., and Prytulak, J. (2022). Magma recharge patterns control eruption styles and magnitudes at Popocatépetl volcano (Mexico). *Geology* 50 (3), 366–370. doi:10.1130/G49365.1

Manley, C. R. (1992). Extended cooling and viscous flow of large, hot rhyolite lavas: Implications of numerical modeling results. *J. Volcanol. Geotherm. Res.* 53 (1-4), 27–46. doi:10.1016/0377-0273(92)90072-L

Martin, V., Pyle, D., and Holness, M. (2006). The role of crystal frameworks in the preservation of enclaves during magma mixing. *Earth Planet. Sci. Lett.* 248 (3–4), 787–799. doi:10.1016/j.epsl.2006.06.030

McVey, B. G., Hooft, E. E. E., Heath, B. A., Toomey, D. R., Paulatto, M., Morgan, J. V., et al. (2020). Magma accumulation beneath Santorini volcano, Greece, from P-wave tomography. *Geology* 48 (3), 231–235. doi:10.1130/G47127.1

Metcalfe, A., Moune, S., Komorowski, J. C., Kilgour, G., Jessop, D. E., Moretti, R., et al. (2021). Magmatic Processes at La Soufrière de Guadeloupe: Insights From Crystal Studies and Diffusion Timescales for Eruption Onset. *Front. Earth Sci.* 9, 617294. doi:10.3389/feart.2021.617294

Morgan, D. J., Blake, S., Rogers, N. W., DeVivo, B., Rolandi, G., Macdonald, R., et al. (2004). Time scales of crystal residence and magma chamber volume from modelling of diffusion profiles in phenocrysts: Vesuvius 1944. *Earth Planet. Sci. Lett.* 222 (3-4), 933–946. doi:10.1016/j.epsl.2004.03.030

Morgan, D. J., Blake, S., Rogers, N. W., De Vivo, B., Rolandi, G., and Davidson, J. P. (2006). Magma chamber recharge at Vesuvius in the century prior to the eruption of AD 79. *Geology* 34 (10), 845–848. doi:10.1130/G22604.1

Müller, T., Dohmen, R., Becker, H. W., Ter Heege, J. H., and Chakraborty, S. (2013). Fe–Mg interdiffusion rates in clinopyroxene: Experimental data and implications for Fe–Mg exchange geothermometers. *Contrib. Mineral. Pet.* 166 (6), 1563–1576. doi:10.1007/s00410-013-0941-y

Nakagawa, K., Nagahara, H., Ozawa, K., Tachibana, S., and Yasuda, A. (2005). "Experimental determination of AlAl–SiMg interdiffusion coefficient in orthopyroxene," in Japan Geoscience Union Meeting (Tokyo), K038–K013. (abstract).

Newhall, C. G., and Dzurisin, D. (1988). *Historical unrest at the large calderas of the world*. US Geological Survey Bulletin, Department of the Interior: US Geological Survey.

Nomikou, P., Parks, M. M., Papanikolaou, D., Pyle, D. M., Mather, T. A., Carey, S., et al. (2014). The emergence and growth of a submarine volcano: The Kameni islands, Santorini (Greece). *GeoResJ* 1, 8–18. doi:10.1016/j.grj.2014.02.002

Nomikou, P., Hübscher, C., Papanikolaou, D., Farangitakis, G. P., Ruhnau, M., and Lampridou, D. (2018). Expanding extension, subsidence and lateral segmentation within the Santorini-Amorgos basins during Quaternary: Implications for the 1956 Amorgos events, central-south Aegean Sea, Greece. *Tectonophysics* 722, 138–153. doi:10.1016/j.tecto.2017.10.016

Ostorero, L., Boudon, G., Balcone-Boissard, H., Morgan, D. J., d'Augustin, T., and Solaro, C. (2021). Time-window into the transcrustal plumbing system dynamics of Dominica (Lesser Antilles). *Sci. Rep.* 11 (1), 11440–11515. doi:10.1038/s41598-021-90831-1

Papale, P., Moretti, R., and Barbato, D. (2006). The compositional dependence of the saturation surface of $H_2O + CO_2$ fluids in silicate melts. *Chem. Geol.* 229, 78–95. doi:10.1016/j.chemgeo.2006.01.013

Parks, M. M., Biggs, J., England, P., Mather, T. A., Nomikou, P., Palamartchouk, K., et al. (2012). Evolution of Santorini Volcano dominated by episodic and rapid fluxes of melt from depth. *Nat. Geosci.* 5 (10), 749–754. doi:10.1038/ngeo1562

Parks, M. M., Moore, J. D., Papanikolaou, X., Biggs, J., Mather, T. A., Pyle, D. M., et al. (2015). From quiescence to unrest: 20 years of satellite geodetic measurements at santorini volcano, Greece. *J. Geophys. Res.* 120 (2), 1309–1328. doi:10.1002/2014JB011540

Petrone, C. M., Bugatti, G., Braschi, E., and Tommasini, S. (2016). Pre-eruptive magmatic processes re-timed using a non-isothermal approach to magma chamber dynamics. *Nat. Commun.* 7, 12946. doi:10.1038/ncomms12946

Preine, J., Karstens, J., Hübscher, C., Nomikou, P., Schmid, F., Crutchley, G. J., et al. (2022). Spatio-temporal evolution of the christiana-santorini-kolumbo volcanic field, aegean sea. *Geology* 50 (1), 96–100. doi:10.1130/G49167.1

Pyle, D. M., and Elliott, J. R. (2006). Quantitative morphology, recent evolution, and future activity of the Kameni Islands volcano, Santorini, Greece. *Geosphere* 2 (5), 253–268. doi:10.1130/GES00028.1

Rasband, W. S. (1997). *ImageJ*. Bethesda, MD: US National Institutes of Health. Available at: http://imagej.nih.gov/ij (Accessed January 10, 2020).

Re, G., Corsaro, R. A., D'Oriano, C., and Pompilio, M. (2021). Petrological monitoring of active volcanoes: A review of existing procedures to achieve best practices and operative protocols during eruptions. *J. Volcanol. Geotherm. Res.* 419, 107365. doi:10.1016/j.jvolgeores.2021.107365

Rizzo, A. L., Barberi, F., Carapezza, M. L., Di Piazza, A., Francalanci, L., Sortino, F., et al. (2015). New mafic magma refilling a quiescent volcano: Evidence from He-Ne-Ar isotopes during the 2011–2012 unrest at Santorini, Greece. *Geochem. Geophys. Geosyst.* 16 (3), 798–814. doi:10.1002/2014GC005653

Saunders, K., Blundy, J., Dohmen, R., and Cashman, K. (2012). Linking petrology and seismology at an active volcano. *Science* 336 (6084), 1023–1027. doi:10.1126/science.1220066

Schwandt, C. S., and McKay, G. A. (2006). Minor- and trace-element sector zoning in synthetic enstatite. *Am. Mineral.* 91 (10), 1607–1615. doi:10.2138/am.2006.2093

Singer, B. S., Le Mével, H., Licciardi, J. M., Córdova, L., Tikoff, B., Garibaldi, N., et al. (2018). Geomorphic expression of rapid Holocene silicic magma reservoir growth beneath Laguna del Maule, Chile. *Sci. Adv.* 4 (6), eaat1513. doi:10.1126/sciadv.aat1513

Smith, R. L., and Bailey, R. A. (1968). "Resurgent cauldrons," in *Studies in Volcanology*. Editors R. R. Coats, R. L. Hay, and C. A. Anderson (Geological Society of America), 116, 613–662. Memoirs Geological Society of America. doi:10.1130/MEM116-p613

Solaro, C., Balcone-Boissard, H., Morgan, D. J., Boudon, G., Martel, C., and Ostorero, L. (2020). A system dynamics approach to understanding the deep magma plumbing system beneath Dominica (lesser antilles). *Front. Earth Sci.* 8, 1–17. doi:10.3389/feart.2020.574032

Sparks, S., Annen, C. J., Blundy, J., Cashman, K., Rust, A., and Jackson, M. D. (2019). Formation and dynamics of magma reservoirs. *Philos. Trans. A Math. Phys. Eng. Sci.* 377 (2139), 20180019. doi:10.1098/rsta.2018.0019

Streck, M. J. (2008). Mineral textures and zoning as evidence for open system processes. *Rev. Mineral. Geochem.* 69 (1), 595–622. doi:10.2138/rmg.2008.69.15

Townsend, M., Huber, C., Degruyter, W., and Bachmann, O. (2019). Magma Chamber Growth During Intercaldera Periods: Insights From Thermo-Mechanical Modeling With Applications to Laguna del Maule, Campi Flegrei, Santorini, and Aso. *Geochem. Geophys. Geosyst.* 20 (3), 1574–1591. doi:10.1029/2018GC008103

Vougioukalakis, G., Sparks, R. S., Druitt, T. H., Pyle, D., Papazachos, C., and Fytikas, M. (2016). Volcanic hazard assessment at santorini volcano: A review and a synthesis in the light of the 2011-2012 santorini unrest. *Bull. Geol. Soc. Greece* 50 (1), 274–283. doi:10.12681/bgsg.11728

Vougioukalakis, G. E., Satow, C. G., and Druitt, T. H. (2019). Volcanism of the South Aegean Volcanic Arc. *Elements* 15 (3), 159–164. doi:10.2138/gselements.15.3.159

Waters, L. E., Andrews, B. J., and Lange, R. A. (2015). Rapid crystallization of plagioclase phenocrysts in silicic melts during fluid-saturated ascent: Phase equilibrium and decompression experiments. *J. Petrol.* 56 (5), 981–1006. doi:10.1093/petrology/egv025

Watts, A. B., Nomikou, P., Moore, J. D. P., Parks, M. M., and Alexandri, M. (2015). Historical bathymetric charts and the evolution of Santorini submarine volcano, Greece. *Geochem. Geophys. Geosyst.* 16 (3), 847–869. doi:10.1002/2014GC005679

Zellmer, G. F., Blake, S., Vance, D., Hawkesworth, C., and Turner, S. (1999). Plagioclase residence times at two island arc volcanoes (Kameni Islands, Santorini, and Soufriere, St. Vincent) determined by Sr diffusion systematics. *Contrib. Mineral. Pet.* 136 (4), 345–357. doi:10.1007/s004100050543

Zellmer, G. F. (2021). Gaining acuity on crystal terminology in volcanic rocks. *Bull. Volcanol.* 83 (11), 78. doi:10.1007/s00445-021-01505-9